Electronic Structure of Manganese Doped Pentacene

A Thesis Submitted to the
College of Graduate Studies and Research
in Partial Fulfillment of the Requirements
for the degree of Master of Science
in the Department of Physics and Engineering Physics
University of Saskatchewan
Saskatoon

By
Tor Møbjerg Pedersen

Permission to Use

In presenting this thesis in partial fulfilment of the requirements for a Postgraduate degree from the University of Saskatchewan, I agree that the Libraries of this University may make it freely available for inspection. I further agree that permission for copying of this thesis in any manner, in whole or in part, for scholarly purposes may be granted by the professor or professors who supervised my thesis work or, in their absence, by the Head of the Department or the Dean of the College in which my thesis work was done. It is understood that any copying or publication or use of this thesis or parts thereof for financial gain shall not be allowed without my written permission. It is also understood that due recognition shall be given to me and to the University of Saskatchewan in any scholarly use which may be made of any material in my thesis.

Requests for permission to copy or to make other use of material in this thesis in whole or part should be addressed to:

Head of the Department of Physics and Engineering Physics
163 Physics Building
116 Science Place
University of Saskatchewan
Saskatoon, Saskatchewan
Canada
S7N 5E2

Abstract

The desire for low cost electronics has led to a huge increase in research focused on organic materials. These materials are appealing due to their unique electrical and material-processing properties and are rapidly being adopted in old and new electronic applications. To create practical devices requires a further understanding of the charge transport properties of the unique anisotropic molecular crystal structures. This work looks at how doping with the transition-metal element manganese can alter the electronic structure of the organic material pentacene. It has been found that using manganese as a dopant provides novel physical characteristics previously not encountered in organic field effect transistors based on pentacene. These organic thin films were characterized using X-ray absorption spectroscopy and the results compared to computational density functional theory analysis.

Acknowledgements

Thanks goes to both my supervisors — Dr. Gap Soo Chang and Dr. Alexander Moewes — for their help and support. Thanks must also go to the other members of the "beamteam" (beamteam.usask.ca) who answered my many questions, and kept things lively in the windowless office.

Thanks to my parents and family for being unique and fully supportive of me. And especially thanks to my wife Dolores for being helpful and encouraging and lovely too.

Thank you, God — Jesus — Holy Ghost.

I dedicate this thesis to Dolores, without your help this never would have happened.

♡

$\varepsilon\acute{\iota}\mu\alpha\iota \quad \varepsilon\rho\omega\tau\varepsilon\upsilon\mu\acute{\varepsilon}\nu\varsigma \quad \mu\alpha\zeta\acute{\iota} \quad \sigma\upsilon$

Contents

List of Tables

List of Figures

List of Abbreviations

BO	Born-Oppenheimer approximation
CMOS	Complementary Metal-Oxide Semiconductor
DFT	Density Functional Theory
DMS	Diluted Magnetic Semiconductor
DOS	Density of States
ECP	Effective Core Potential
EXAFS	Extended X-ray Absorption Fine Structure
FWHM	Full Width Half Maximum
GGA	Generalized Gradient Approximation
GTO	Gaussian Type Orbital
GMR	Giant Magnetoresistance
HOMO	Highest Occupied Molecular Orbital
IP	Ionization Potential
I-V	Current-Voltage
LCAO	Linear Combination of Atomic Orbitals
LDA	Local Density Approximation
LMO	Localized Molecular Orbital
LUMO	Lowest Unoccupied Molecular Orbital
MO	Molecular Orbital
MOSFET	Metal-Oxide Semiconductor Field-Effect Transistor
n-doped	(negative) donor doped semiconductor
NEXAFS	Near Edge X-ray Absorption Fine Structure
OFET	Organic Field Effect Transistor
OLED	Organic Light Emitting Diode
OTFT	Organic Thin Film Transistor
p-doped	(positive) acceptor doped semiconductor
PDOS	Partial (or Projected) Density of States
PFY	Partial Fluorescence Yield
RIXS	Resonant Inelastic X-ray Scattering
RKKY	Ruderman-Kittel-Kasuya-Yosida interaction
RT	Room Temperature
SCF	Self-Consistent Field
SE	Schrödinger equation
SO	Spin-Orbit
TEY	Total Electron Yield
TFY	Total Fluorescence Yield
XA	X-ray Absorption
XANES	X-ray Absorption Near Edge Structure
XAS	X-ray Absorption Spectroscopy
XE	X-ray Emission
XES	X-ray Emission Spectroscopy

Chapter 1

Introduction

Spin-electronics (*spintronics*) is a burgeoning research field in condensed matter physics that is attempting to create functional electronic devices based on the electron's spin degree of freedom, in addition to its charge. The basic ingredients needed to create a functioning device are the ability to create, sustain, control, and detect a current of spin polarized carriers [1]. The technological impact of this emerging field will have a large effect on the future of the electronics industry [2]. There are many practical devices and applications that scientists and engineers are envisioning based on spintronics research. Some of the areas being focussed on are: *magnetic random access memory* (MRAM), spin-based transistors, mass-storage devices, ultra-fast switches, and multifunctional chips that could provide computation, storage, and communication on a single chip [3].

The one breakthrough that could lead to a revolution in everyday life — in the same vein as the transistor did 60 years ago — would be the development of a quantum computer. Quantum computation based on *qubits* (quantum bits), uses the principle of superposition to store information in a way that allows computations to be performed in parallel as opposed to sequentially. Using ingenious quantum algorithms, it allows one to perform 2^n computations for every n qubits, essentially scaling computations exponentially [4]. Possible applications would include modeling a realistic system of many self-interacting electrons [5].

Research in spintronics has reached the level where there are several different avenues that material scientists are focusing on to reach these goals. One avenue involves finding new applications for ferromagnetic metallic alloys — this field also goes by the heading of *magnetoelectronics*. One recent shining example of success in

this area was the development of spin valves which use the *giant magnetoresistance* (GMR) effect [6–8]. These GMR read-heads are used in almost all current computer hard drives and have led to the enormous increase in hard drive areal densities in the past decade. MRAM is also nearing completion for commercial applications and products could begin appearing within the year [9, 10].

Another route is to develop traditional semiconducting materials that can generate and carry the necessary spin-polarized currents. These materials are generally labelled as *diluted magnetic semiconductors* (DMS). The discovery of ferromagnetic (III,Mn)V semiconductors around 15 years ago has led to concerted research in trying to find a DMS possessing a sufficiently high *Curie temperature* (T_c) for practical applications [11, 12]. Since a huge microelectronic infrastructure is in place utilizing traditional semiconducting materials (i.e. silicon, gallium arsenide, etc.), commercial devices could be developed in a very short time-frame [13].

Another broad category of materials being investigated are organic semiconductors. The monetary drive for using organic materials is that they possess key economic advantages over traditional semiconducting materials, such as: ease of processing, structural flexibility, the possibility for large surface-area applications, and a reduction in manufacturing costs [14]. Another benefit would be helping to eliminate the use of harmful heavy elements and chemicals used in computers. One sometimes overlooked result, but possibly also the most important in terms of the health of the planet, is that spintronic devices would consume drastically less electric power [3, 15–17]. Current CMOS based logic and memory chips are now reaching the point where the increase in power required for nanoscale designs are hampering further developments in the field [18]. The fundamental physical properties that make organic molecular materials attractive are the weak *spin-orbit* and *hyperfine* interactions. This allows for increased spin-coherence times for the polarized electrons [19].

One of the as-yet unrealized applications envisioned for spintronics is the development of a spin-based transistor which would enable quaternary operation and the possible development of a robust *room-temperature* (RT) quantum computer [20]. There are several competing methods that would enable the realization of this spin-

transistor. One method uses a quantum pumping effect to create separation of pure spin currents [21]. Another method is to develop RT ferromagnetic semiconducting heterostructures [12]. The latter method is the general approach taken in this research, albeit using molecular materials to create an *organic field effect transistor* (OFET).

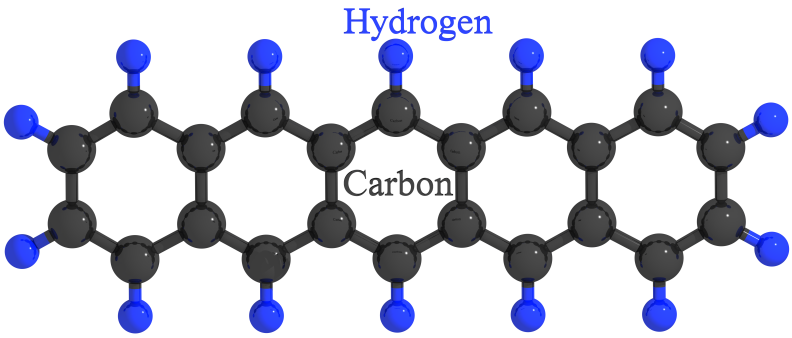

Figure 1.1: Chemical structure of pentacene showing the carbon (dark grey) and hydrogen (blue) atoms.

One method to create the desired properties for the spin-transistor is to dope the semiconductor with transition metals, such as manganese (Mn) or cobalt (Co) [12]. We have done this with pentacene and used synchrotron-based *X-ray absorption* (XAS) and *X-ray emission spectroscopy* (XES) to study how these impurities change the magnetic and electrical properties of the material. Figure 1.1 shows the atomic representation of pentacene.

XAS and XES are element and site specific techniques which enable us to determine where in the organic material the dopants reside, and to what molecular orbitals the dopants are bonding with [22]. In aiding this process, *density functional theory* (DFT) calculations are performed that allow us to assign values to the *highest occupied molecular orbital* (HOMO) and *lowest unoccupied molecular orbital* (LUMO) states [19]. The energy gap between the HOMO and LUMO levels serves as an indication of the excitability of the material — in essence determining how suitable the material is for practical applications. The specific goal of this research is to determine how the magnetic dopants affect the HOMO-LUMO gap in the material.

By answering this question — through mapping out the electronic structure — it becomes possible to provide a concrete physical explanation to the unique and novel transistor properties observed in the doped pentacene heterostructures examined.

Chapter 2 takes a look at the underpinnings of spintronic research with some background information on organic materials with specific attention placed on pentacene. The specific research goals are given in chapter 3. The focus then shifts to the experimental and theoretical techniques used in mapping out the electronic structure in chapter 4. The results are presented in chapter 5, with conclusions and recommendations presented in chapter 6.

Chapter 2

Pentacene in Device Applications

2.1 Organic Electronics

With the discovery in 1963 of conducting polypyrroles by chemically doping the organic material, it took another 15 years before much interest was generated in these materials [23]. In 1977, doped polyacetylene was shown to be a conducting polymer [24]. This result in contrast generated considerably more interest and resulted in the people involved receiving the Nobel Prize in Chemistry in 2000 — not withstanding some controversy [25]. Since then, research in organic materials has undergone an enormous growth that continues unabated to this day.

Organic materials have been used extensively in the fabrication of everyday electronics for many years. Traditionally they have only been used in the processing steps of the long-established semiconducting materials as photoresists or as passive insulators [26]. They have, for the most part, taken a back seat as active components in functioning electronic devices. That has changed drastically in the past several years with the development of *organic light emitting diodes* (OLED) used in display applications. Currently, organic materials are being used in applications requiring conduction of current, and emission of visible light [26]. OFETs are also tantalizingly close to being used in commercial applications [27].

Organic molecular materials are also interesting in that they possess inherently unique electronic properties not found in other materials. For organic materials the band structure is derived from *molecular orbitals* (MO) using approximations based on the *linear combination of atomic orbitals* (LCAO) approach. Pentacene is part of the oligoacene family of polycyclic aromatic hydrocarbons, which are composed of

conjugated molecules — meaning they have alternating single and double bonds. In pentacene ($C_{22}H_{14}$), the carbon atoms are each joined to three others, which results in one delocalized electron occupying a p_z-orbital. These π-MOs overlap with neighbouring orbitals creating π-bonds. These overlapping π-bonds give rise to delocalized electrons which are free to move within the molecule and are largely responsible for the intramolecular conduction. Figure 2.1 visualizes these ideas. Typically this ef-

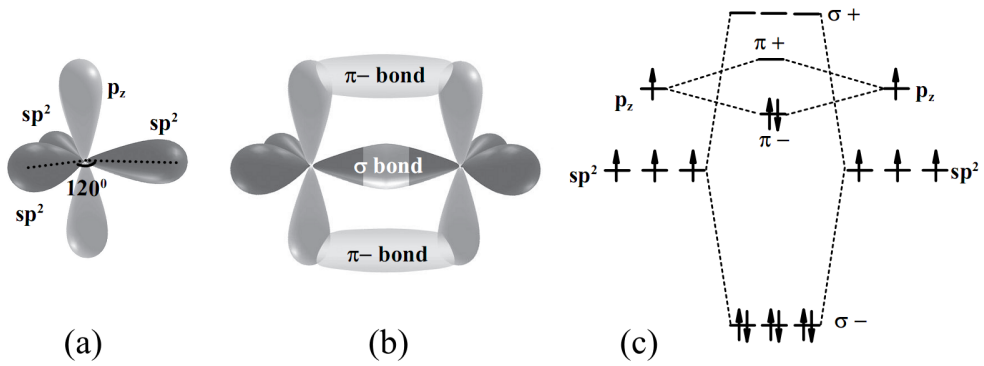

Figure 2.1: The construction of pentacene's carbon-MOs: (a) the sp^2 and p_z orbitals for a C atom, (b) the creation of a π-bond between two C atoms, (c) energy level diagram showing the formation of π and σ bonds in carbon. Figure adapted from ref. [28].

fect is anisotropic as the overlapping MOs usually occur in the plane of the molecule. This result is highly desirable as it gives rise to weak spin-orbit and hyperfine interactions within the organic molecules. Combining this with the weak *van der Waals* interaction between adjacent molecules, one can get spin coherence times that are much greater than in DMS systems. This leads to greater transport distances for the spin-polarized carriers [19]. One negative aspect of organic materials is that the spin carrier density is usually comprised of holes versus electrons. Holes typically have much shorter spin coherence lifetimes than electrons do. This detriment can be overcome by various doping methods to create n-doped organic semiconductors [29].

Pentacene has become somewhat of the *de facto* standard in organic molecular conductors as it has so far consistently demonstrated the highest hole mobilities for organic molecular crystals [30]. Mobility (μ) is defined in terms of the drift velocity

($\mathbf{v_d}$) of electrons (or holes) per unit electric field ($\mathbf{E}$). Typically it takes the form shown in equation (2.1.1) given below:

$$\mathbf{v_d} = \mu \mathbf{E} \tag{2.1.1}$$

Increased mobilities directly translate into higher switching speeds for transistors based on *complementary metal-oxide semiconductor* (CMOS) logic [31]. If organic materials want to compete with amorphous silicon in display applications the mobility should approach $\sim 1\ cm^2/V \cdot s$ with switching speeds of $\sim 10^8\ Hz$. Pentacene has satisfied both these criteria [32] while also demonstrating higher mobilities approaching 1000 $cm^2/V \cdot s$ exhibited for conduction through a single molecule [30]. So far the most promising results for developing a functioning spintronic device have come from heterostructures based on Mn-doped pentacene.

2.2 OFET Device Operation

An organic field effect transistor works similarly to a normal *metal-oxide-semiconductor FET* (MOSFET) [33]. It is a three terminal device with contacts labelled gate, drain, and source. See figure 2.2 for the details. The current-flow through the device occurs

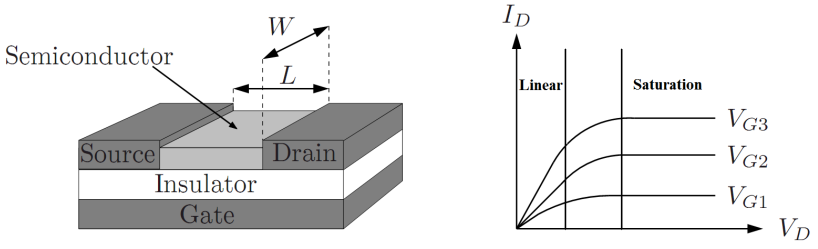

Figure 2.2: OFET structure is shown on the left where W is the width and L is the length of the conducting channel. The graph on the right is a typical I-V curve showing the linear and saturation regions for increasing gate voltages (V_{Gi}). Figure adapted from ref. [34].

at the organic semiconductor-insulator interface and is controlled by the voltage applied to the gate terminal. Essentially it works like a capacitor with the gate voltage determining the density of charge carriers accumulating at the interface, which in

turn leads to a conducting channel between the source and drain [35, 36]. For low drain voltages V_D — which occur within the linear regime indicated in figure 2.2 — the drain current can be given by:

$$I_D = \frac{W}{L}\mu C_i(V_G - V_T)V_D \tag{2.2.1}$$

Where W and L are the channel width and length, μ is the mobility, C_i is the capacitance of the insulator, V_G is the gate voltage, and V_T is the threshold voltage at which the transistor turns on. This is only valid for $V_D \ll V_G$ [35, 37]. For higher V_D voltages the drain current is independent of the drain voltage — the so-called saturation regime — and the drain current is given by:

$$I_D = \frac{W}{2L}\mu C_i(V_G - V_T)^2 \tag{2.2.2}$$

From these equations values for the mobility can be determined. The real-life operation of OFETs depend to a large degree on the quality of the interface between the organic semiconductor and the dielectric [38, 39]. This is due to the fact that almost all of the charge accumulates in the first layer of the device [35]. Much research has gone into determining how to enhance the physical properties at this interface. Another factor limiting the performance of OFETs is the charge injection difficulties encountered with the metal contacts and the organic material [40–42]. It is found that charge traps occur at this interface and interface dipoles are created due to the mismatch between the Fermi levels of the metal and semiconductor [43–45]. Electrons have a higher energy barrier to overcome for charge injection (versus holes), therefore the majority of OFETs operate as p-type transistors [34, 44, 46].

2.3 Conduction Mechanisms in Small Organic Materials

In talking about possible conduction paths in pentacene, it is important to clarify what physical form the pentacene takes that one is studying. Some of the various forms of pentacene that researchers have studied are: amorphous, single crystals,

and isolated single molecules [47, 48]. There are several different isomorphs of pentacene single crystals, and at times material scientists have not been aware of these differences and how they affect the results found [49]. Most polymers grow as an amorphous phase during thin film fabrication. Pentacene in contrast quite readily forms pure single crystals during thin film growth [49]. This simplifies modelling of the material and helps in determining the intrinsic transport properties as one can now make use of the various symmetries present. In many cases, the transport properties that one measures are significantly affected by the way in which the crystalline pentacene interfaces with the materials joining it. This can result in charge traps, defects, and localized gap states that can reduce the mobility of the device up to a factor of ten [50].

Even though conducting organic materials have been researched for over 25 years, there still remain large gaps in understanding concerning how charge transport occurs in these materials [51]. Organic materials can vary in size from large strands of DNA, to polymers, to "small" molecules. "Small" molecular compounds are generally considered to be ones that have a specific molecular weight and can form well-defined crystal structures - of which pentacene is a member. The bonding between individual molecules in the organic crystal occurs through weak van der Waals forces that decrease as $1/R^6$ — versus the $1/R^2$ dependence found in covalently bonded inorganic semiconductors (with R being the intermolecular spacing) [52]. This causes many of the electronic properties (essentially the HOMO and LUMO gap) of the material to primarily stem from the electronic structure of each individual molecule. This simplifies DFT calculations as one can subsequently use an isolated molecule instead of scaling up to the complete crystal structure. The negative consequence of the weak van der Waals bonding is that it creates narrower electron bands and stronger electron-phonon coupling [53]. As a result the charge carriers are believed to be polaronic in nature [54].

A polaron is an electron in the conduction band (or a hole in the valence band) that either polarizes or distorts the surrounding lattice such that as it moves through the crystal it brings along with it an accompanying "phonon cloud" [55]. In small

organic molecules, the polaron strongly influences nearby local geometry (as opposed to a long range effect) and can be classified as a "small polaron." These polarons interact strongly with local defects and create difficulties in determining the intrinsic electron mobility [56]. At room temperatures the thermal excitations present can be comparable to the width of the narrow conduction band of the material [51]. This can lead to a change in the charge transport mechanism from a band description involving polarons to incoherent hopping between localized states [57]. Essentially the electrons cannot "hop" from their quasi-bound states unless they get additional energy from surrounding phonons. Since this process is temperature dependent, the mobility does scale with increasing temperature. The cross-over from band-like transport to hopping conduction is also an area requiring more research.

The crux of the matter is that accounting for electron-electron correlation is difficult enough without having the added challenge of including electron-phonon interactions as well. In spite of these challenges, some progress has been made recently — both experimentally and theoretically. The development of pure samples has led to some intrinsic charge measurements for surface conduction in organic field effect transistors (OFET) [54]. On the theoretical side, a model for phonon-assisted charge-carrier transport has been developed — based on work done by Holstein and Peierls [53].

2.4 Modified Pentacene OFETs

Pentacene, used as the semiconducting layer in OFETs, has so far exhibited the highest hole mobilities to date for organic materials — with the most recent result (2007) achieving between $15-40\ cm^2/V\cdot s$ [33]. This result was found in a functional OFET design, and is significant, as the previous record for mobility ($\sim 35\ cm^2/V\cdot s$) was for conduction through a single molecular crystal of pentacene [33]. Electron mobilities in pentacene OFETs are considerable smaller and much research is aimed at finding ways to increase these values [58]. The goal is to create n-type conduction comparable to the mobilities for p-type conduction. This would enable ambipolar

transistors to be made allowing for the creation of complementary integrated circuits. This could allow one to fabricate a fully organic computational device [37, 59].

Pentacene exhibits stable amphoteric doping — given the right conditions — and to date dopants that have been used are: Li, Na, K, Ca, Rb, I, and Cs [60–73]. Most of the dopants are alkaline metals and are used as they have high electronegativities. Another method used is to chemically modify the pentacene structure using various additive groups [58, 74–76]. Fluorine and cyanide are two examples of chemicals that have been used in this capacity [58, 75, 76]. Figure 2.3 shows the end result of the fluorination process used to create perfluoropentacene. As with doping, this

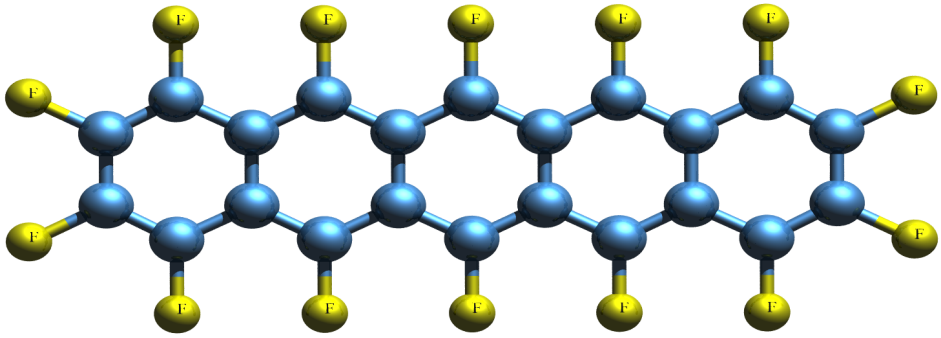

Figure 2.3: The hydrogen atoms have been substituted with fluorine atoms (yellow) to create perfluoropentacene.

technique attempts to tune the frontier energy levels by substituting in electron-withdrawing groups [37]. Other techniques that have been used to create n-type behaviour are: using ultraviolet light to modify the dielectric interface [59, 77], plasma-enhanced deposition [78], creating heterostructures using separate materials for the hole and electron conduction channels [79–81], and modifying the metal contacts with organic materials [82]. So far ambipolar operation has been limited to only a handful of situations — not necessarily due to an intrinsic limit with organic semiconductors but most likely due to a result of the trapping of electrons in the commonly used SiO_2 gate oxide [46].Only very recently have devices been demonstrated that exhibit both the n- and p-type behaviour desired [37, 83, 84]. To date, there have been no known attempts to create ambipolar transistors using

transition-metal atoms as dopants.

2.5 Organic Spintronics

Research in spintronics has undergone considerable growth in the past ten years. The majority of the research so far has focused on using traditional semiconducting materials. Recently though, with organic electronic devices being used in commercial applications, more consideration has been given to these materials to see what additional benefits, or novel functionalities, they may provide over the more entrenched electronic materials. There are two main areas that molecular materials hold key advantages over inorganic ones. One is due to the intrinsic properties of organic materials that allow for longer spin coherence times due to both the weak spin-orbit and hyperfine coupling mechanisms present. The other is the unique configurations possible when coupling the organic materials to magnetic metals [85].

There are many possible devices envisioned that make use of the spin property of the electron. Some of the more common ones are the spin-FET, magnetic bipolar transistor, spin qubits, spin diode, spin filter, and spin LED. For a good overview of these devices and for an in-depth discussion of spintronic fundamentals see references [1, 86]. This section will focus on the properties of organic materials that are advantageous for some of these devices.

Spin-orbit Interaction

The relativistic *spin-orbit* (SO) interaction couples the spin $\boldsymbol{S}$ with the orbital angular momentum $\boldsymbol{L}$. The result is a new total angular momentum $\boldsymbol{J}$ given by:

$$\boldsymbol{J} = \boldsymbol{L} + \boldsymbol{S} \tag{2.5.1}$$

This interaction creates orbital magnetism and couples the spin system to the extended structure allowing energy and angular momentum exchange [87]. The SO Hamiltonian is written in the following form:

$$\mathcal{H}_{\mathrm{SO}} = \xi_{nl}(r)\boldsymbol{L} \cdot \boldsymbol{S} \tag{2.5.2}$$

Where $\xi_{nl}(r)$ is defined to be:

$$\xi_{nl}(r) = -\frac{e\hbar^2}{2m_e^2c^2}\frac{1}{r}\frac{d\phi(r)}{dr} \tag{2.5.3}$$

with $\phi(r)$ being the electrostatic potential, m_e the mass of the electron, and c the speed of light. If one takes $\phi(r)$ to be due to the nuclear charges $(+Ze)$, then $\xi_{nl}(r)$ becomes:

$$\xi_{nl}(r) = \frac{Ze^2\hbar^2}{8\pi\epsilon_0 m_e^2c^2r^3} \tag{2.5.4}$$

The expectation value $\langle\xi_{nl}(r)\rangle$ of equation (2.5.3) is labelled the spin-orbit parameter ζ_{nl} and has dimensions of energy.

The SO interaction is quite small in comparison to the exchange interaction, but it is responsible for much of the loss in spin-coherence as it gives rise to spin precession. The magnitude of the SO effect depends on Z and as a consequence it is small for organic materials which consist primarily of carbon. Table 2.1 compares the SO parameter ζ_{nl} for several semiconductors in comparison to carbon (in diamond form). As can be seen ζ_{nl} for carbon is less than one third of the value for silicon

Table 2.1: Spin-orbit valence band splitting for select semiconductors. Values obtained from ref. [85].

Semiconductor	ζ_{nl} (meV)
C	13
Si	44
GaP	80
InP	111
Ge	290
GaAs	340
InAs	380
GaSb	750
InSb	980

and results in a considerable increase in spin lifetime.

Hyperfine Interaction

The hyperfine interaction which is due to the coupling of the electron and nuclear spins also plays a role in the decoherence of electrons. If the nucleus undergoes a random spin flip, it can also cause the electron to change its spin direction. The hyperfine Hamiltonian is given below:

$$\mathcal{H}_{\text{hyp}} = \sum_{i}^{N} A_i \mathbf{S_i^{NUC}} \cdot \mathbf{S} \tag{2.5.5}$$

where A_i is the coupling strength between the spin operator $\mathbf{S_i^{NUC}}$ for nucleus i, and the spin operator $\mathbf{S}$ for the electron. Carbon has a minimal hyperfine interaction as the main isotope (98.93% ^{12}C) has a nuclear spin of zero (i.e. $\mathbf{S^{NUC}} = 0$). Therefore, since the delocalized π-MOs associated with the carbon atoms are responsible for much of the charge (and spin) transport in organic molecules the hyperfine interaction is considerably reduced. This is especially true for conjugated molecules because the π-MOs are composed of C p_z orbitals which have their nodal plane coincident with the molecular plane [86].

Spin Relaxation Time and Length

The spin lifetime τ_s is a transport parameter that allows one to define the scale of coherence for the electrons in spintronic devices [88]. The equation below shows its constituent parts [86].

$$\frac{1}{\tau_s} = \frac{1}{\tau_{\uparrow\downarrow}} + \frac{1}{\tau_{\downarrow\uparrow}} \tag{2.5.6}$$

The $\tau_{\uparrow\downarrow}$ is the average spin-flip time for an up-spin to change to a down-spin, and $\tau_{\downarrow\uparrow}$ is the reverse of this. This spin relaxation time also sets the length scale for coherent spin transport. Equation 2.5.7 below, which is applicable for semiconductors that can be approximated by a degenerate Fermi gas, shows this relationship:

$$l_s = \sqrt{\frac{\tau_s}{4e^2\rho(E_F)\gamma}} \tag{2.5.7}$$

where $\rho(E_F)$ is the density of states at the Fermi level E_F, and γ is the resistivity of the non-magnetic material. For the non-degenerate case l_s is given by,

$$l_s = \sqrt{\frac{k_B T \tau_s}{2ne^2\gamma}} \tag{2.5.8}$$

Where k_B is Boltzmann's constant, T is temperature, and n is the number of carriers. For more detail regarding the derivation of equations (2.5.7) and (2.5.8) see references [89, 90].

Semiconductors exhibit lifetimes much longer than in metals and organic materials are even better in that regard. For silicon a lower bound on the spin lifetime has been found to be $\sim$1 ns with potentially much larger values close to 7 ns [1, 88]. For n-GaAs it has been found that spin lifetimes can approach $\sim$100 ns for n-doped samples. Considering the reduction of the SO and hyperfine effects the values obtained for the spin lifetime in organic materials can be much higher than in semiconductors. In pentacene, τ_s is estimated to be between 10^{-6} and 10^{-5} seconds [91, 92].

Mn-doped Pentacene

Our work has focused on creating spin polarization of carriers in manganese doped pentacene. The Mn dopant atoms are used to modify pentacene's electronic structure, with the goal of creating a room-temperature magnetic semiconductor.

The reason for using Mn is that it has partially filled $3d$ electronic orbitals, which create ligands (shared electrons through covalent bonding) with the organic molecule. These ligands modify the HOMO and LUMO states of the molecule and cause splitting of the five degenerate d-orbitals (d_{z^2}, $d_{x^2-y^2}$, d_{xy}, d_{xz}, and d_{yz}) into orbitals of high and low energy, depending on the coordination environment surrounding the metal ion. This modification of the d-orbitals can create local magnetic moments in the material. This can give rise to magnetism through Mn-Mn interactions or the creation of carrier mediated ferromagnetism through optical or electrical means — for example by means of the *Ruderman-Kittel-Kasuya-Yosida* (RKKY) interaction [47, 93].

Chapter 3

Research Hypothesis

3.1 Research Questions

The question posed by this research is to see how the Mn dopant atoms affect the HOMO and LUMO energy levels of the pentacene OFETs. The hypothesis is that the Mn atoms will contribute to the DOS of both the HOMO and LUMO levels of the pentacene molecule. This will result in some form of hybridization (i.e. charge transfer) between these MOs, and the band gap of the OFET should decrease, resulting in more metallic behaviour. Measuring these OFETs using XAS and XES is one method that can be used to answer this question. By doing further XA and DOS calculations using DFT, it may be possible to develop and verify an underlying model.

3.2 Justification for this Research

Pentacene exhibits the highest hole mobilities (up to $15 - 40\, cm^2/V \cdot s$) in OFET devices [33]. Therefore if it were possible to increase the n-type conduction up to p-type levels, complementary semiconducting circuits could be fabricated. This would essentially create functioning organic computational devices. Most of the research involving doped pentacene has focused on using alkali elements, and to date transition metal elements have been ignored. The reason for this is due to the challenge of introducing metal dopants into organic materials without modifying the structural properties of the material significantly [37, 94]. As will be seen in the results section, the addition of the Mn atoms has a minimal impact on the pentacene

crystal structure. This result provides a way to investigate new doping materials and strategies.

3.3 Goals of this Research

The primary goal of this research is to determine in what capacity the Mn atoms affect the transport properties of the OFETs. By using Mn-dopants to modify the HOMO/LUMO energy gap it becomes possible to tailor specific properties of a device for a designed purpose. If it can be determined with reasonable accuracy how these properties are modified by the dopants, it will be possible to create complementary organic semiconducting circuits. This is a requirement for the development of fully organic computational devices based on CMOS logic. The comparison of experiment with theory (computations) will also allow a deeper understanding of the usefulness of various MO models and their applicability for predicting device properties and tailoring performance characteristics.

Chapter 4

Soft X-ray Spectroscopies

4.1 Theory of Soft X-ray Spectroscopies

In characterizing magnetically doped organic semiconductors it is useful to determine the HOMO and LUMO states as it gives an indication of how the dopant atoms affect the electronic structure of the material and thereby its useful semiconducting properties. The HOMO and LUMO states are analogous to the valence and conduction bands in traditional semiconductors. Determining the HOMO/LUMO gap can be used as an indicator of the photon-excitability of the molecule.

XAS and XES are ideally suited for directly mapping out these HOMO and LUMO states [95]. XAS directly probes the local partial density of unoccupied states while XES probes the local partial density of occupied states [96]. These complementary techniques provide a practical means of detailing the local electronic structure of the material - which can change significantly due to the presence of any magnetic impurities [52].

4.1.1 X-ray Absorption Spectroscopy

X-ray Absorption Techniques

X-ray absorption (XA) occurs when a photon is absorbed by a core level electron, and the electron is then excited to either a higher unoccupied state or the continuum. An XAS spectrum records the XA intensity versus the incoming photon energy. Figure 4.1 shows a model XA spectrum. Labels in the figure show the three different energy ranges which are focused on depending on what one is investigating. *X-ray absorption*

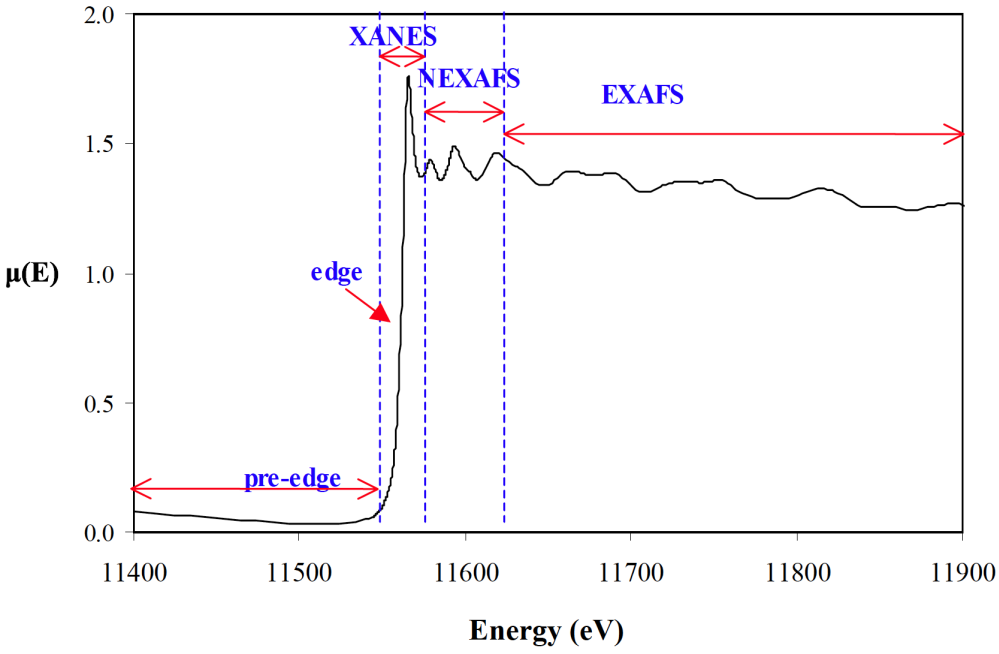

Figure 4.1: Normalized XA spectrum showing regions of interest. Figure adapted from ref. [97].

near-edge structure (XANES) is measured around 30 eV of the binding energy of the atomic site of interest. It provides information about the site symmetry and valency of the atom probed. *Near-edge X-ray absorption fine structure* (NEXAFS) is loosely classified to be between 10 and 70 eV above the absorption edge. It is usually used in studying chemisorbed molecules on surfaces as it provides information about the intramolecular bond lengths and orientations of the molecule [22]. *Extended X-ray absorption fine structure* (EXAFS) goes from around 50 to 1000 eV above the absorption edge. The electrons in this region have high kinetic energy and therefore are usually scattered by nearest neighbour atoms. The technique therefore provides local structural information concerning the excited atom, and conversely when measuring free atoms (noble or monatomic gases) one will not see the fine structure oscillations present in the spectra. In summary, the items of interest that one can determine using XAS are the following: element specific DOS, molecular

orientation, local atomic structure, lattice parameters, and the length, orientation, and nature of chemical bonds [98]. For our work the techniques that provide us with the most pertinent information are XANES and NEXAFS.

X-ray Absorption Physics

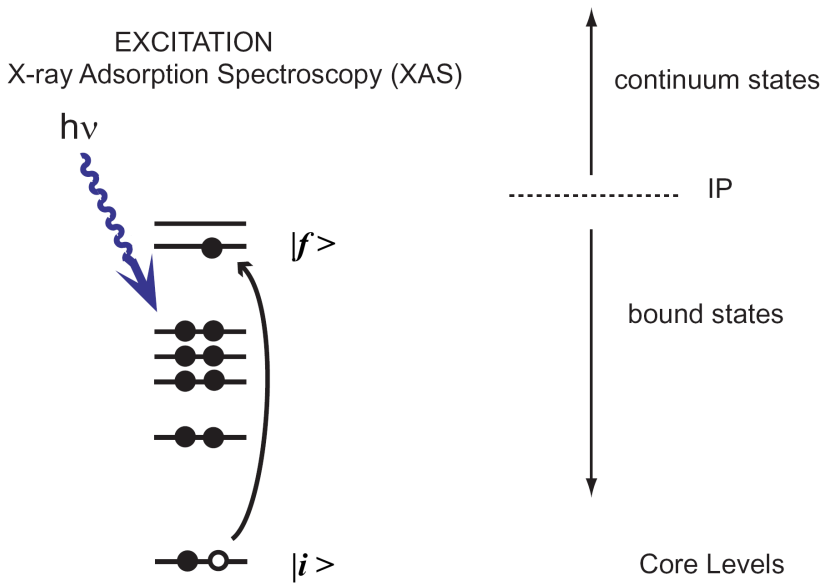

Figure 4.2: Schematic of the core-hole creation process showing the initial state $|i\rangle$ and final state $|f\rangle$. Adapted from ref. [99].

The XA and XE transition probabilities are calculated by considering a time-dependent perturbation of the material by the incoming X-rays. The incoming photons induce transitions between the initial state $|i\rangle$ and the final excited state $|f\rangle$ — as shown in figure 4.2. XA is a first-order process, so the transition from $|i\rangle$ to $|f\rangle$ occurs in one step with no intermediate states. XA occurs on an attosecond timescale for ionization events $\sim$10 eV above the ionization potential, allowing the so-called *sudden approximation* to hold. The sudden approximation allows one to assume that the electronic transition possesses a single-electron character and occurs rapidly in relation to the relaxation times of the other "passive" electrons. The transition probability per unit time (up to first order) for an absorption event is given

below:

$$T_{if} = \frac{2\pi}{\hbar}|\langle f|\hat{\mathcal{H}}_{int}|i\rangle|^2\rho(\varepsilon_f) \tag{4.1.1}$$

where $|i\rangle$ and $|f\rangle$ are the wavefunctions of the combined photon plus atom system, and $\rho(\varepsilon_f)$ is the density of final states [87]. $\hat{\mathcal{H}}_{int}$ is the interaction Hamiltonian given by the product of the momentum operator $\hat{\mathbf{p}}$ and the vector potential operator $\hat{\mathbf{A}}$ according to the equation below:

$$\hat{\mathcal{H}}_{int} = \frac{e}{m_e}\hat{\mathbf{p}}\cdot\hat{\mathbf{A}} \tag{4.1.2}$$

The core shell of any atom being probed is strongly localized. The element specificity comes directly from the characteristic binding energies of the elements, and partly from the localization of the XA event. One can view the XA process as a way to decompose the molecular orbitals into their respective atomic orbitals.

Dipole Approximation

The wavelength of the incoming radiation for soft X-rays ($\lambda \geq 1.2\ nm$) is much larger than the atomic dimensions ($\mathbf{r} \simeq 0.01\ nm$ for the $2p$ core shell), this allows one to make a *dipole approximation* for the incoming radiation [87]. Essentially it assumes that the perturbing electric field is constant over the volume of the atom that is undergoing excitation. The X-ray absorption cross-section, in the dipole approximation, is given below,

$$\sigma^{abs} = 4\pi^2\alpha\hbar\omega|\langle f_{el}|\boldsymbol{\epsilon}\cdot\hat{\mathbf{r}}|i_{el}\rangle|^2\rho(E_f) \tag{4.1.3}$$

where α is the fine structure constant, $\hat{\mathbf{r}}$ is the dipole operator, $\boldsymbol{\epsilon}$ is the unit photon polarization vector, and $\rho(E_f)$ is the density of final states per unit energy which depends on the normalization of the electronic wavefunctions $|f_{el}\rangle$ and $|i_{el}\rangle$. The absorption cross-section measures the number of electrons excited per unit time, divided by the number of incoming photons per unit area, per unit time. It has dimensions of cm^2 or given in units of "barns", where $1\ barn = 10^{-24}\ cm^2$.

Selection Rules

The validity of the dipole approximation gives rise to several electric dipole selection rules for transitions between the initial and final states in the XA and XE process. These selection rules are based on the ones obtained for a one-electron atom having azimuthal (l), magnetic (m), spin (s), and total angular momentum (j) quantum numbers. The list below shows the possible values allowed for radiative (dipole) transitions,

$$\begin{aligned} \Delta l &= \pm 1 \\ \Delta m &= 0, \pm 1 \\ \Delta s &= 0 \\ \Delta j &= 0, \pm 1 \end{aligned} \tag{4.1.4}$$

where Δ is defined as the difference between the initial and final quantum states.

Broadening Factors

There are several broadening factors one has to consider when analyzing X-ray spectra. The main ones being instrumental, core-hole lifetime, and final-state (excited electron) lifetime broadening factors. These all have an impact on the sharpness of spectral features. Instrumental broadening is due to the measuring conditions of the experimental set-up. Contributing factors to this effect can come from the optical resolution of the beamline, the mechanical resolution of monochromator components, and the duration of measurements. All of these effects are combined together into a single broadening factor called the instrumental resolving power ($E/\Delta E$). It is a systematic instrumental effect and depends on the incoming energy of the photons. To incorporate the effect into calculated spectra it is modeled with a Gaussian function with the standard deviation derived from the resolving power [100].

During X-ray absorption the molecule undergoes a transformation from the initial state to a resonant final state. The full width of the resonance Γ is determined according to Heisenberg's uncertainty principle,

$$\Gamma \simeq \frac{\hbar}{\tau} \tag{4.1.5}$$

where τ is the lifetime of the final state. Equation (4.1.5) can be further reduced by separating τ into two contributions [22]:

$$\frac{1}{\tau} = \frac{1}{\tau_e} + \frac{1}{\tau_h} \tag{4.1.6}$$

where τ_e is the excited electron lifetime, and τ_h is the core-hole lifetime. The core-hole lifetime for carbon has a width of $\Gamma \simeq 0.1\, eV$ which translates into a characteristic lifetime in the range of $10^{-15} - 10^{-14}$ seconds [22]. The resonantly trapped electron has a much larger width of $\Gamma \simeq 10\, eV$ corresponding to a shorter lifetime in $10^{-17} - 10^{-16}$ second range. As a result the core-hole will have an effect on the trapped electron. These lifetime broadening effects are modeled with Lorentzian functions in calculated spectra [101, 102].

4.1.2 X-ray Emission Spectroscopy

XES is a photon-in/photon-out process that occurs when the core hole created in an X-ray absorption event is "refilled" by a higher energy electron — usually coming from the valence band. The difference in energy between the valence electron and the core hole is transferred to the emission of a photon of that energy. This photon is then detected and analysed with a spectrometer. XES therefore results in a spectrum showing the emission intensity as a function of the emission energy. Since the core hole created during XA is localized it results in a detailed snapshot of the local electronic structure around the element specific atomic site of interest. In other words it probes the local partial density of occupied states [103]. Figure 4.3 shows a schematic of this non-resonant process. The transition probability for this process is given in equation (4.1.7) below — where the dipole approximation has been used to simplify the expression.

$$T_{if} = \frac{2\pi}{\hbar} |\langle f | \boldsymbol{\epsilon} \cdot \hat{\mathbf{r}} | i \rangle|^2 \rho(\varepsilon_f) \tag{4.1.7}$$

As for XA, $|i\rangle$ and $|f\rangle$ are the initial and final wavefunctions of the system and $\rho(\varepsilon_f)$ is the density of final states.

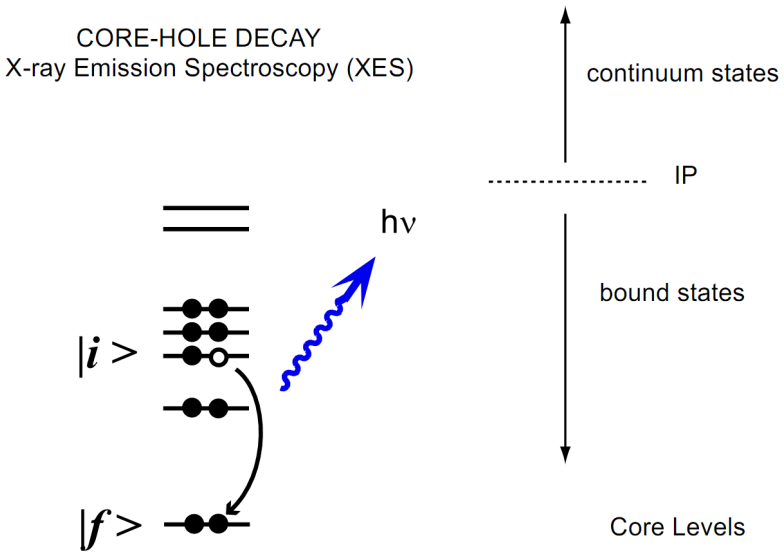

Figure 4.3: Schematic of the XE process showing the initial $|i\rangle$ and final $|f\rangle$ states. The final state in non-resonant XE is a valence ionized atom or molecule. Adapted from ref. [104].

4.2 Experimentation Techniques

4.2.1 Synchrotron Sources

A synchrotron is an experimental facility which makes use of photons to measure various properties of materials. Currently synchrotrons are in their "third generation" and are designed for high radiation output by using insertion devices such as undulators, wigglers, and bending magnets. When electrons are accelerated close to the speed of light they emit radiation in the form of highly energetic (GeV) photons. To maintain the acceleration of the electrons and the subsequent emission of photons, the electrons are confined to a circular path using magnetic fields generated from insertion devices around the storage ring for the electrons. These photons can be tuned to a very narrow energy window creating a highly focussed and nearly monochromatic source with exceptional spectral brightness - also sometimes called brilliance. Spectral brightness is defined as the photon flux impinging on the sample per unit area, per unit solid angle, per unit relative energy bandwidth. Equation

(4.2.1) below clarifies this:

$$B_{\Delta\omega/\omega} = \frac{\Delta P}{\Delta A \cdot \Delta\Omega \cdot \Delta\omega/\omega} \tag{4.2.1}$$

ΔP is the power radiated from an area ΔA into a solid angle $\Delta\Omega$ within a relative spectral bandwidth $\Delta\omega/\omega$ [105]. The brilliance obtained allows experiments to have three principal advantages over smaller laboratory set-ups: higher spatial resolution, higher coherence, and higher spectral resolution [106]. All of the spectra presented in this thesis were performed at the Advanced Light Source (ALS) at the Lawrence Berkeley National Laboratory in the USA. Use was made of the Soft X-Ray Fluorescence (SXF) spectrometer located on beamline 8.0.1 [107]. The electronic charge density distribution of a material directly determines the size and shape of a molecule and its proclivity toward bonding. In essence, it determines nearly all of the physical and chemical properties of the material. Since this negative charge occurs in real space it is something which can be both directly and indirectly measured using various techniques. Some of the experimental methods used currently in condensed matter research that use synchrotrons are *X-ray absorption* and *emission spectroscopy* (XAS and XES), *X-ray excited optical luminescence* (XEOL), *photoemission electron microscopy* (PEEM), *angle-resolved photoelectron spectroscopy* (ARPES), and *X-ray magnetic circular dichroism* (XMCD), among many others.

4.2.2 Beamline Setup

Beamline 8.0.1 uses an undulator to create photons possessing small angular divergence and a narrow spectral width. The undulator has 89 poles with a period of 5.0 cm, with the first, third, and fifth, harmonics being useful. The first harmonic covers an energy range from $70 - 250$ eV, with higher harmonics covering energies up to 1200 eV by adjusting the undulator gap. Figure 4.4 shows the schematic layout of the beamline. The radiation coming from the undulator is focused onto the entrance slit by a water-cooled SiC vertical condensing mirror. The interchangeable and rotatable spherical gratings monochromatize the incoming light depending on the selected energy range from the undulator. These water-cooled, holographically

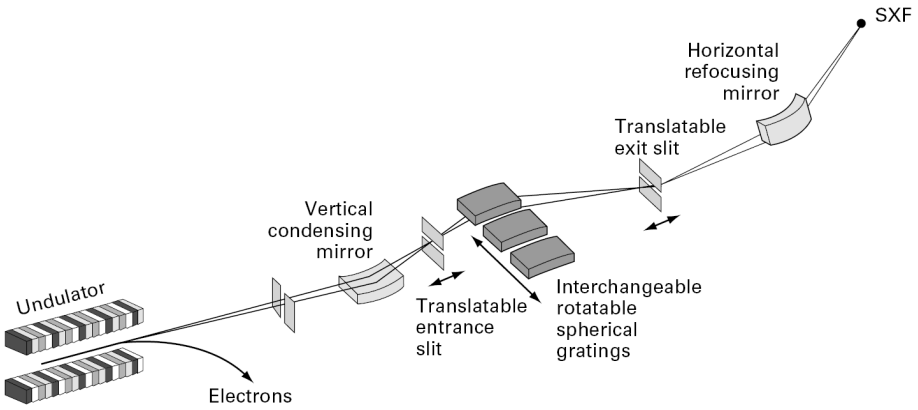

Figure 4.4: Layout of Beamline 8.0.1. showing the movable entrance and exit slits. Figure adapted from [107].

ruled, spherical gratings have rulings of 150, 380, and 925 lines/mm. By satisfying Rowland geometry with the movement of the entrance and exit slits the optimal focusing conditions are met. The horizontal refocusing mirror narrows the spot size for the SXF endstation. The resultant spot size of 100 $\mu m \times 100\ \mu m$, has an estimated photon flux of 10^{13} photons per second, giving a resolving power of 10000 [108].

4.2.3 X-ray Absorption Measurements

Beamline 8.0.1 is equipped to measure XAS using three different experimental methods: *total electron yield* (TEY) *partial fluorescence yield* (PFY) and *total fluorescence yield* (TFY). Each method has strengths and weaknesses that depend primarily on the type of sample one is measuring and the energy resolution desired. Since all three methods yield results which are proportional to the X-ray absorption coefficient, it becomes necessary to understand the situations where each method excels. All three methods have different sample-to-background (or signal-to-noise) ratios that also play a part in the suitability of which method to use. For our samples the TEY method was the most suitable, and the results presented use TEY exclusively.

Total Electron Yield

During an X-ray absorption process the incoming photon creates a core hole. This empty core hole will either be refilled by a non-radiative process, such as Auger decay, or a radiative process, such as X-ray fluorescence. These are two of the competing methods for the soft X-ray energy range of interest. The two routes have different time-scales creating different relative yields, which in turn are a function of the atomic number Z. For low-Z materials like carbon, and also for L-shell excitation of atoms with $Z < 90$ the Auger decay channel dominates. This makes TEY a good method as the signal-to-noise ratio is generally better than for fluorescent yield methods. Figure 4.5 shows these two processes. Total electron yield measures the

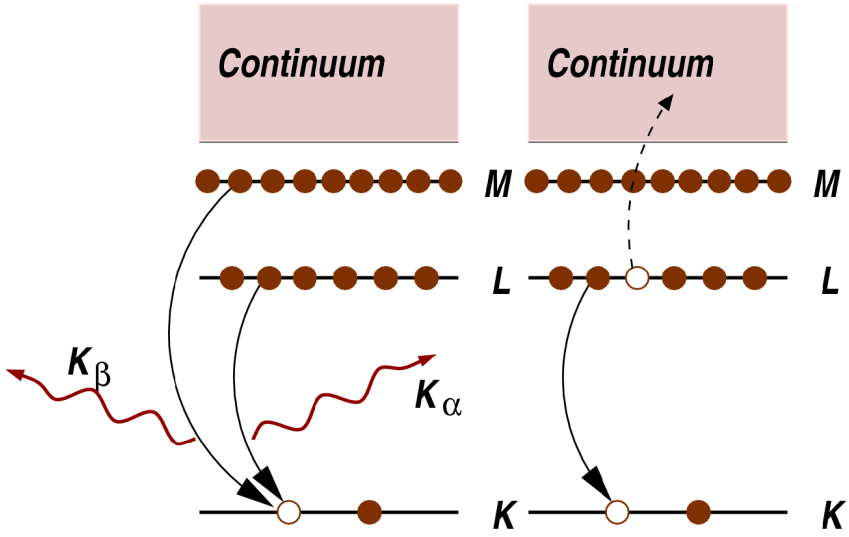

Figure 4.5: Diagram of an absorption process showing two of the competing methods for measuring X-ray absorption spectra. The left hand side of the figure shows the radiative decay process. The core hole is filled with an electron from either the L- or M-shell, with radiation (K_α or K_β) being emitted. The right side shows the Auger decay process, where the electron escapes into the continuum. Figure from ref. [109].

total number of electrons that leave the sample, either through primary excitation processes (photoelectrons) or secondary processes, such as Auger decay. The sample holder is connected to ground and the current flowing through the wire to neutralize the ionized sample is measured with an ammeter. This is the only electrical con-

nection to the sample holder. Therefore the measured current is proportional to the absorption coefficient. In comparison to hard X-rays, the soft X-ray penetration depth is considerably shorter. For carbon the penetration depth varies between 5–100 nm (depending on the incidence angle) for $\lambda \approx 0.4\ nm$ [22, 105] . Even so, this is considerably greater than the escape depth of the excited electrons, as they experience electron-electron, electron-plasmon, and electron-phonon interactions which all limit the electron scattering length [22]. As the photoelectrons scatter through the material it creates an electron cascade effect. Only some of these electrons will have sufficient energy to overcome the work function of the material and contribute to the electron yield signal. Any excited electrons created below a certain depth L will have insufficient energy to overcome the potential energy barrier of the surface. Figure 4.6 shows this effect schematically. This results in the electron yield

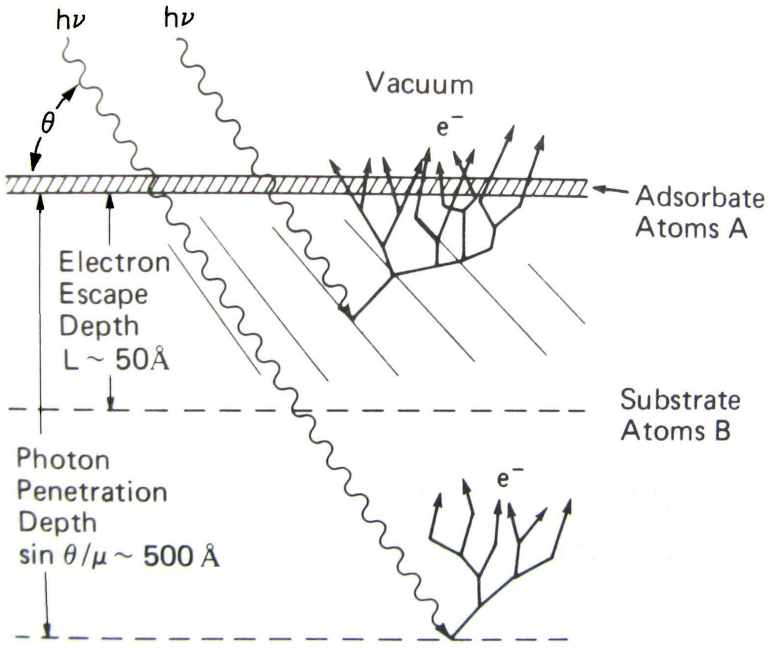

Figure 4.6: The incoming photon (hν) is absorbed by the material, giving rise to an electron cascade. Only excited electrons within a certain depth L escape the material and contribute to the electron yield signal. Figure adapted from ref. [22].

signal being somewhat surface sensitive in comparison to fluorescent yield signals as photons have an order of magnitude greater escape depth.

Normalization and Energy Calibration

The experimental set-up has a fine gold mesh that is placed along the beamline close to the sample holder such that after the beam passes through it, its next stop becomes the sample holder. As the beam passes through this highly transparent gold mesh a current is generated that is measured with a picoammeter. The absorption signal is then normalized by dividing the measured signal by the gold mesh current. Normalization allows one to account for any fluctuations that may be present in the incident beam current. It also ensures that the measured spectrum is independent of absorption that may occur with beamline components that precede the sample — such as the various monochromator gratings and mirrors.

Energy calibration for X-ray spectroscopy measurements are essential, as the beamline is a mechanical and optical device with moving components. This introduces slight errors in the energy positions of the measured spectra. To account for these variations it is necessary to always measure a reference sample that possesses well-established values for the prominent peaks in its spectrum. This reference sample's spectrum is linearly shifted up or down in energy to match the known energy values. This energy offset is then subsequently applied to all other measured spectra done at the same excitation energy.

4.2.4 X-ray Emission Measurements

The SXF endstation consists of a grating emission spectrometer utilizing a photon counting multi-channel plate (MCP) area detector. The MCP is mounted on a XY-θ motion table. This is located perpendicular to the incident beam with a fixed entrance slit located near the sample holder manipulator (see Figure 4.7). The ultra-high vacuum (UHV) sample chamber has XYZ-θ motion with provisions for cryogenic and elevated temperature use. To cover the energy ranges of interest (40–1000 eV), the spectrometer utilizes four interchangeable gratings, this ensures that the entire emission spectrum can be recorded without needing to scan the MCP detector. XAS and XES measurements can be performed immediately after each other without the

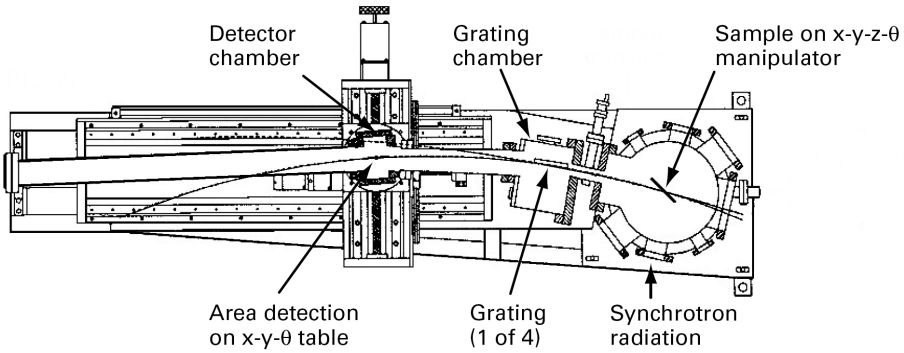

Figure 4.7: Schematic of the SXF spectrometer endstation showing the entrance slit, gratings, and detector all lying along the Rowland circle geometry. Figure from ref. [108].

need to take the sample out of vacuum. For further details see references [107] and [108]. As XES is a photon-in/photon-out process it ensures that the sample is free of any charging effects which can occur with some of the XA measurement techniques. This allows one to use the technique on a large range of samples — both conducting and insulating — and can probe the bulk material due to the larger escape depth for photons.

4.2.5 Sample Fabrication

The pentacene and Mn-doped pentacene samples were prepared in South Korea using chemical vapour deposition. The pentacene organic layer was thermally evaporated onto a doped silicon substrate with a 100 nm thick SiO_2 gate-oxide layer. The Mn-doped samples were prepared under similar conditions with Mn thermally evaporated concurrently with the pentacene. The evaporation temperature was set at 160 °C. The thickness of the deposited organic layer was controlled using a calibrated quartz-crystal monitor, and set to 40 nm. After depositing the pentacene layer, a 10 nm thick gold capping layer was applied to prevent any oxygen uptake by pentacene. The doping concentration for Mn (4 or 8% by volume) is determined using a combination of the evaporation rate ($0.1\text{Å}/s$) and the quartz-crystal monitor.

4.3 Theoretical Methods

4.3.1 Density Functional Theory

The Schrödinger Equation

Much of the work presented here, such as: determining ground state energies; simulating X-ray spectra; performing geometry optimizations; all require the use of methods based on quantum mechanics. All of the theoretical methods stem from using forms of the *Schrödinger equation* (SE), which is given below in its most general form [110].

$$\hat{\mathcal{H}}(t)|\Psi(t)\rangle = i\hbar\frac{\partial}{\partial t}|\Psi(t)\rangle \tag{4.3.1}$$

Where $\hat{\mathcal{H}}(t)$ is the time-dependent Hamiltonian, $|\Psi(t)\rangle$ is the state vector at time t, and $\hbar$ is the reduced Planck's constant. The time-independent Hamiltonian for a system of interacting electrons and atomic nuclei can be given by the following general equation [111].

$$\begin{aligned}\hat{\mathcal{H}} = &-\sum_{I=1}^{P}\frac{1}{2M_I}\nabla_I^2 - \sum_{i=1}^{N}\frac{1}{2m}\nabla_i^2 + \frac{1}{2}\sum_{I=1}^{P}\sum_{J\neq I}^{P}\frac{Z_I Z_J}{|\mathbf{R_I}-\mathbf{R_J}|} \\ &+\frac{1}{2}\sum_{i=1}^{N}\sum_{j\neq i}^{N}\frac{1}{|\mathbf{r_i}-\mathbf{r_j}|} - \sum_{I=1}^{P}\sum_{i=1}^{N}\frac{Z_I}{|\mathbf{R_I}-\mathbf{r_i}|}\end{aligned} \tag{4.3.2}$$

Where P are the nuclear coordinates given by the set $\mathbf{R} = \{\mathbf{R_I},\ I = 1,\ldots,P\}$, and N are the electronic coordinates given by $\mathbf{r} = \{\mathbf{r_i},\ i = 1,\ldots,N\}$, Z_I are the nuclear charges and M_I are the masses. The equation is given in atomic units with $\hbar = e = \frac{1}{4\pi\epsilon_0} = 1$. This Hamiltonian operator breaks down the total energy contributions of the extended system into components associated with the electrons and nuclei, and their interactions with each other. The first two terms are due to kinetic energy of the nuclei and electrons, and the last three terms deal with potential energy contributions. Applying this Hamiltonian to the time-independent SE (4.3.3) allows one to determine many of the physical properties of a material.

$$\hat{\mathcal{H}}\Psi_n(\mathbf{R},\mathbf{r}) = \mathcal{E}_n\Psi_n(\mathbf{R},\mathbf{r}) \tag{4.3.3}$$

Solving (4.3.3) gives the energy of the system, where $\mathcal{E}_n$ are the energy eigenvalues, and the wavefunctions (or eigenstates) are given by Ψ_n. Using various other operators in place of the Hamiltonian will give you any other physical property you might be interested in. The disadvantage with this approach is that the SE cannot easily be decoupled into a set of independent equations and therefore one is left with attempting to solve an equation involving $3(P+N)$ coupled degrees of freedom [111]. For a realistic solid-state system there will be on the order of $10^{23}-10^{26}$ particles — resulting in a many-body wavefunction that quickly becomes intractable. To solve this many-body problem it becomes necessary to resort to approximations that can deal with the enormous number of particles involved. This led to the development of the classical nuclei approximation — also called the *Born-Oppenheimer* (BO) approximation, and subsequently to *density functional theory* (DFT).

The Born-Oppenheimer Approximation

This approximation treats the nuclei as classical particles allowing one to separate the electronic and nuclear degrees of freedom. The BO approximation is valid for many realistic situations as the electron to nuclear mass ratio (m/M) is always smaller than the nucleus by at least 2×10^4. Essentially the electrons move almost instantaneously in relation to the thermally vibrating nuclei, making it reasonable to assume that the electrons remain in their ground state [112]. Equation (4.3.4) below condenses (4.3.2) and enables us to show more clearly which terms are affected by the BO approximation.

$$\hat{\mathcal{H}} = \hat{\mathcal{T}}_n + \hat{\mathcal{T}}_e + \hat{\mathcal{V}}_{nn} + \hat{\mathcal{V}}_{ee} + \hat{\mathcal{V}}_{ne} \tag{4.3.4}$$

The $\hat{\mathcal{T}}$-terms are kinetic energy, $\hat{\mathcal{V}}$-terms are potential energy, and n and e are indices for the nuclei and electrons respectively. So in the BO approximation the $\hat{\mathcal{T}}_n$ term can be neglected as the nuclei are assumed to be stationary in regards to electronic motion. The nuclear repulsion $\hat{\mathcal{V}}_{nn}$ term is treated as a constant for a given geometry. And the correlation in the attractive nuclear-electron potential term ($\hat{\mathcal{V}}_{ne}$) is removed. The end result being that one is left with a Hamiltonian that is only dependent on

the electronic degrees of freedom (i.e. coordinates), with the nuclear coordinates entering the equation as parameters. This formulation does not necessarily help the situation much on its own, as one still has similar scaling issues when increasing the number of atoms. But what it does allow is the application of DFT to the problem as it satisfies the constraints that are inherent with DFT.

Density Functional Theory

Hohenberg and Kohn's approach was to develop DFT as an exact theory of a many-body system that applies to any system of interacting particles in an external potential [113]. For solid state systems the external potential is taken to be the nuclear potential ($\mathcal{V}_{nn}$), and the interacting particles are the electrons — although the theorems have been generalized by Levy and Lieb to apply to a wider range of systems and conditions [114]. DFT is based on two simple theorems which are stated below [113]:

1. In any system of interacting particles in an external potential $v_{\text{ext}}(\mathbf{r})$, the potential $v_{\text{ext}}(\mathbf{r})$ is determined uniquely, except for an additive constant, by the ground state electron density $\rho_o(\mathbf{r})$.

2. The ground state energy of the interacting electron gas is a unique functional of $\rho_o(\mathbf{r})$ for any external potential $v_{\text{ext}}(\mathbf{r})$.

Thereom 1 in essence says that it is possible using only the electron's ground-state density $\big(\rho_o(\mathbf{r})\big)$, to determine all of the physical properties of the system. This leads to an enormous simplification as now the electron density is the basic variable — which only depends (in three dimensions) on a scalar field of three variables [115]. Theorem 2 says that the functional $E[\rho]$ is sufficient to determine the exact ground state energy E_o. The problem is that this exact functional has so far not been determined. The usefulness of the theorem is the fact that there is a variational principle for finding the charge density. The next step in the process is to make use of these theorems, which Kohn and Sham did in 1965.

Kohn-Sham Equations

Kohn and Sham proposed to simplify the Hamiltonian operator by assuming that one had a system of non-interacting particles. This would allow one to express the Hamiltonian as a sum of single-particle operators. Now the problem of finding the ground state electron charge density simplifies to solving a set of single-particle eigenvalue equations. The so-called *Kohn-Sham* (KS) equations are given below:

$$\left(-\frac{1}{2m}\nabla^2 + V_{\text{eff}}(\mathbf{r})\right)\psi_i(\mathbf{r}) = \epsilon_i^{KS}\psi_i(\mathbf{r}), \qquad \epsilon_1^{KS} \leq \epsilon_2^{KS} \leq \cdots, \tag{4.3.5}$$

$$V_{\text{eff}}(\mathbf{r}) = V_{\text{ext}}(\mathbf{r}) + V_H(\mathbf{r}) + V_{XC}(\mathbf{r}) \tag{4.3.6}$$

The $\{\psi_i\}$ are called KS-eigenstates and the $V_{\text{eff}}(\mathbf{r})$ is the effective potential felt by each independent electron. The ϵ_i^{KS} are the corresponding KS-energies. In equation (4.3.6) the $V_{\text{ext}}(\mathbf{r})$ is the external potential due to any applied electric field and also includes the nuclear potential term. $V_H(\mathbf{r})$ is called the Hartree potential and is due to the electrostatic potential generated from the electronic charge density $\rho(\mathbf{r})$ given by solving Poisson's equation:

$$-\nabla^2 V_H(\mathbf{r}) = \rho(\mathbf{r}) \tag{4.3.7}$$

to get,

$$V_H(\mathbf{r}) = \int \frac{\rho(\mathbf{r}')}{|\mathbf{r} - \mathbf{r}'|} d\mathbf{r}' \tag{4.3.8}$$

The $V_{XC}(\mathbf{r})$ term is the exchange-correlation potential and equals the functional derivative of the exchange correlation energy $E_{XC}[\rho(\mathbf{r})]$:

$$V_{XC}(\mathbf{r}) = \frac{\delta E_{XC}[\rho(\mathbf{r})]}{\delta \rho(\mathbf{r})} \tag{4.3.9}$$

The charge density is calculated from the occupied KS-states according to:

$$\rho(\mathbf{r}) = \sum_{i \text{ occupied}} |\psi_i(\mathbf{r})|^2 \tag{4.3.10}$$

with the condition that,

$$\langle \psi_i | \psi_i \rangle = 1 \tag{4.3.11}$$

Finally the ground state energy E_o can be found from the solution of equation (4.3.5)

$$E_o = \sum_{i=1}^{N} \epsilon_i + \frac{1}{2} \int \frac{\rho(\mathbf{r})\rho(\mathbf{r}')}{|\mathbf{r} - \mathbf{r}'|} d\mathbf{r} d\mathbf{r}' + E_{XC}[\rho(\mathbf{r})] - \int \rho(\mathbf{r}) V_{XC}(\mathbf{r}) d\mathbf{r} \tag{4.3.12}$$

The exact form of the exchange-correlation energy is not known, so the usefulness of DFT depends on finding approximations for the functional $E_{XC}[\rho(\mathbf{r})]$ that are simple and accurate [110]. This has led to various forms of the $E_{XC}[\rho(\mathbf{r})]$ functional with two of the most popular being the *local density approximation* (LDA) and the *generalized gradient approximation* (GGA).

LDA and GGA

The LDA is an exchange-correlation functional that depends only on the local electron density. It assumes the electrons have a local density that is the same as the density for a uniform electron gas. This allows the $E_{XC}[\rho(\mathbf{r})]$ functional to be approximated as;

$$E_{XC}^{LDA}[\rho(\mathbf{r})] \approx \int \varepsilon_{XC}[\rho(\mathbf{r})]\rho(\mathbf{r}) d\mathbf{r} \tag{4.3.13}$$

Neglecting correlation gives us a simple form for the exchange energy,

$$\varepsilon_X[\rho(\mathbf{r})] \approx -\frac{3e^2}{2\pi} \big(3\pi^2 \rho(\mathbf{r})\big)^{\frac{1}{3}} \rho(\mathbf{r}) \tag{4.3.14}$$

which is clearly only dependent on the local electronic density.

The GGA goes one step further than the LDA by taking into account the gradient of the density in the functional dependence of the energy operator, as the equation below shows:

$$E_{XC}^{GGA}[\rho(\mathbf{r})] = \int f\big(\rho(\mathbf{r}), \nabla\rho(\mathbf{r})\big) d\mathbf{r} \tag{4.3.15}$$

With f being a universal function of the electronic densities and their gradients. There are several versions of the GGA, all of which are parametrized somewhat differently. The specific form of the GGA used in the work presented in this thesis will be covered in the next section concerning StoBe — the DFT computer program used to model the molecules studied.

4.3.2 StoBe

StoBe (Stockholm-Berlin — named after where the principle authors reside) is a DFT based program that is particularly suited for comparison with spectroscopic techniques such as NEXAFS and XES. The program was initially based on the deMon (Density of Montréal) code written by D.R. Salahub at the University of Montréal [116]. StoBe uses an iterative *self-consistent field* (SCF) approach to the solution of the previously mentioned KS-equations. It does this using a *linear combination of atomic orbitals* (LCAO), specifically using *Gaussian type orbitals* (GTO) as the basis sets used to form the KS-orbitals.

The program outputs results in Hartree atomic units (*a.u.*). In this natural unit system the following physical constants are normalized to unity:

$$e = \hbar = m_e = \frac{1}{4\pi\epsilon_0} = 1 \tag{4.3.16}$$

where e is the charge of an electron, $\hbar$ is the reduced Planck's constant, m_e is the mass of an electron, and ϵ_0 is the permittivity of free space. It follows that a_0 (the Bohr radius) also becomes unity. The conversion factor between S.I. units and atomic units is given below:

$$1\ a.u. = \frac{e^2}{4\pi\epsilon_0 a_0} = \frac{\alpha\hbar c}{a_0} \approx 27.211\ eV \approx 4.3597 \times 10^{-18}\ J \tag{4.3.17}$$

where c is the speed of light in vacuum, and α is the fine structure constant given by:

$$\alpha = \frac{e^2}{4\pi\epsilon_0\hbar c} \tag{4.3.18}$$

Basis Sets

Equation (4.3.19) below shows how the KS-states (or orbitals) from equation (4.3.5) are built-up using these GTO basis functions.

$$\psi_i = \sum_{j=1}^{N} a_j \chi_j \tag{4.3.19}$$

The a_j are the coefficients for the orbital basis functions χ_j, and the number N determines the size of the so-called basis set which is used. The a_j are the varying

parameters during the iterative DFT calculations while the functions are kept static. The χ_j are derived from using an integral representation for the exponential functions that occur in wavefunctions for the atomic orbitals. As an example, the equation below shows a hydrogen-like $1s$ function expanded in a Gaussian basis:

$$e^{-\xi r} = \frac{\xi}{2\sqrt{\pi}} \int_0^\infty s^{\frac{3}{2}} e^{-\frac{\xi^2}{4s} - sr^2} ds \tag{4.3.20}$$

The limits are subsequently reduced to s_1 and s_2 (from $0 \rightarrow \infty$) through minimizing the cut-off errors to an acceptable value [117]. The next step involves transforming the integral into a sum over a regular grid allowing for easier use of computation algorithms.

The basis sets are generally defined by the number of s-, p-, and d-type functions used to approximate the "real" s, p, and d AOs. The general notation $(n_s/n_p/n_d)$ is used for this purpose. To account for polarization effects the element in question will have additional angular functions added. For example, hydrogen will have p-type functions included, and not simply be based on s-type functions. All of the GTO basis sets used in StoBe are commonly used basis sets developed by Sigeru Huzinaga in 1965 [118], with refined numerical parameters from ref. [119].

The molecules are also represented by *auxiliary* basis sets which are used to fit the electron density, and the exchange and correlation terms [119]. The notation StoBe uses for these basis sets is similar to the GTO notation. The general form is $(k_s^C, l_{s,p,d}^C; m_s^{xc}, n_{s,p,d}^{xc})$, where k_s^C is the number of s-type functions, and $l_{s,p,d}^C$ determines the number of s-, p-, and d-type functions sharing the same exponents in the Gaussian basis "expansion" for the Coulomb potential. m_s^{xc} and $n_{s,p,d}^{xc}$ constitute the exchange/correlation set with the numbers taking the same meaning as for the charge density basis set [120]. All the calculations used an A5 auxiliary basis set based on the so-called *triple-ζ valence plus polarization* (TZVP) orbital basis set. The triple-ζ stands for the number of radial functions used, with more than three functions (i.e. quadruple-ζ) not changing results appreciably for molecular systems [119]. The only exception to this are the hydrogen basis sets, which used three contracted s-functions with one augmented p-function — resulting in a double-ζ valence

Table 4.1: Basis sets for the atoms used in StoBe calculations

Element	GTO Basis	Auxiliary Basis
Hydrogen	(311/1)	(3,1;3,1)
Carbon	(7111/411/1)	(5,2;5,2)
Cobalt	(63321/531/311)	(5,5;5,5)
Manganese	(63321/531/311)	(5,5;5,5)

plus polarization (DZVP) basis set. Table 4.1 is a summary of the different basis sets used for the elements in this project.

In addition, StoBe uses *augmented* basis sets to improve the results when calculating excited states. This is the so-called even-tempered basis set technique. These basis sets have an atom-centered basis augmented with atomic-like wave functions surrounding the spherical regions of the nuclei [111]. This allows flexible basis functions giving rise to a greater level of accuracy. The downside is that they require more resources and are technically more complicated as any redundancies in the final basis set need to be checked for and removed. In StoBe the augmented basis is placed on the atom being excited, with the large diffuse basis set consisting of over one hundred *s*-, *p*-, and *d*-type functions [121]. In addition to this large diffuse basis the excited atom is also initially modeled with a good molecular basis set to obtain the bound molecular orbitals. In StoBe this is done with the IGLO-III basis set by Kutzelnigg, which allows for better modeling of the relaxation effects in the inner orbitals [117, 121].

Oscillator Strengths

The *oscillator strength* f is the energy integral of the XA cross-section (equation (4.1.3)) and accounts for the intensity of the resonances observed in the measured spectra. f is defined below:

$$f = 4\pi^2 \alpha \hbar \omega |\langle f|\boldsymbol{\epsilon} \cdot \hat{\mathbf{r}}|i\rangle|^2 \tag{4.3.21}$$

where $|f\rangle$ and $|i\rangle$ are volume normalized to unity. The total oscillator strengths for both discrete and continuum transitions satisfy the Thomas-Reiche-Kuhn sum rule. Simply put, it states that for an electron in an atom or molecule the sum of all the oscillator strengths for all transitions is unity [22]. It follows that the total oscillator strength for a transition is equal to the total number of electrons N in the molecule — as shown below:

$$\sum_n f_n + \int_{IP}^{\infty} \frac{df(E)}{dE} dE = N \tag{4.3.22}$$

The first term in equation (4.3.22) accounts for the discrete resonances below the ionization potential (IP), and the second term accounts for the intensity above the IP. The sum rule enables one to relate the calculated oscillator strengths with the experimental peak area, as the area under the curve of a $df(E)/dE$ versus E plot is proportional to the number of electrons in an atomic or molecular system.

Theoretical X-ray Spectra

StoBe's main advantage over other *ab initio* DFT programs are the specific implementations done to model inner-shell spectroscopies. It can determine energy differences between the core to both valence and unoccupied states, by using the calculated dipole transition probabilities. With the use of these values it becomes possible to produce theoretical X-ray spectra. The theory is based on the *transition state* (TS) method, which uses a half-occupied core hole on the excited atom. This approach was originally developed by Slater for the multiple scattering Xα method [122, 123], but has shown good results for NEXAFS and XES of small molecules [121, 124]. One of the benefits of the TS method is that it includes a large part of the relaxation energy (up to second order), which is generally accurate enough for the majority of core ionization/excitation problems [121].

As there are 22 carbon atoms in pentacene the core orbitals tend toward delocalization in the calculations. This can cause convergence issues when determining the correct energy values for these atoms. To account for this, so-called *effective core potentials* (ECP), or pseudopotentials, are used for all equivalent atoms not undergoing excitation. This keeps the core orbital localized on the specific atom being excited

[125]. An ECP allows one to account for the core electrons in the DFT calculation by replacing the nuclear charge of the atom, with an effective charge that includes the core electrons. That is,

$$Z_{eff} = Z - Z_{core} \tag{4.3.23}$$

where Z_{core} is the charge associated with the core electrons. For carbon $Z_{core} = 2$, resulting in $Z_{eff} = 4$. This allows one to reduce the number of electrons that are treated explicitly and decreases the computation time considerably. The downside is that using the ECP approximation can introduce an error up to 0.2 eV (for the binding energy), but for carbon atoms it is well below 0.05 eV [125].

In StoBe the oscillator strengths are calculated for each transition and then summed. These oscillator strengths are determined from the x-, y-, and z-components of the dipole transition moment, as shown for the cartesian x-component below [116]:

$$f_x = \langle \psi_f | x | \psi_{core} \rangle \tag{4.3.24}$$

where ψ_f and ψ_{core} are the final and core KS-orbitals. The total oscillator strength is then computed with the following equation [116, 124],

$$f_{total} = \frac{2}{3} E_{\text{exc}} (f_x^2 + f_y^2 + f_z^2) \tag{4.3.25}$$

where E_{exc} is the excitation energy (in Hartree units) and f_x, f_y, f_z are the cartesian dipole transition moments, with the result given in atomic units. One can now take these oscillators strengths for each atom, sum them, and apply broadening values that mimic experimental conditions. This results in a final spectrum that can be compared with the experimental XA or XE spectra.

Implementation

As the DFT algorithms scale on the order of N^3 — there is an artificial limit to the number of atoms, N, one can model. Trying to model more than ∼200 atoms in StoBe results in prohibitive computational time with current hardware. StoBe has default limits set to 140 atoms, 3800 primitive/1900 contracted Gaussians for orbitals, and 3800 primitive Gaussians for the auxiliary functions. It was necessary

to change these limits in the program, by doing some minor code modifications to allow some of the results presented here to work.

All of the calculations performed used the gradient corrected exchange functional by Becke [126] given in the equation below (in atomic units):

$$E_X^{GGA}[\rho_\sigma(\mathbf{r})] = E_X^{LDA} - \beta \sum_\sigma \int \rho_\sigma^{4/3} \frac{x_\sigma^2}{(1 + 6\beta x_\sigma \sinh^{-1} x_\sigma)} d^3\mathbf{r} \tag{4.3.26}$$

where β is a constant, ρ_σ is the spin density, and x_σ is a dimensionless ratio given by,

$$x_\sigma = \frac{|\nabla \rho_\sigma|}{\rho_\sigma^{4/3}} \tag{4.3.27}$$

A correlation-energy functional by Perdew was used for all the calculations and is given below [127].

$$E_C[\rho(\mathbf{r})] = E_C^{LSD} + \int \frac{e^{-\Phi} C(\rho) |\nabla \rho|^2}{D \rho^{4/3}} d^3\mathbf{r} \tag{4.3.28}$$

where D equals,

$$D = 2^{1/2} \left[\left(\frac{1+\zeta}{2} \right)^{5/3} + \left(\frac{1-\zeta}{2} \right)^{5/3} \right]^{1/2} \tag{4.3.29}$$

with,

$$\zeta = \frac{\rho_\uparrow - \rho_\downarrow}{\rho_\uparrow + \rho_\downarrow} \tag{4.3.30}$$

Φ is given by,

$$\Phi = 1.745 \tilde{f} \left[\frac{C(\infty)}{C(\rho)} \right] \frac{|\nabla \rho|}{\rho^{7/6}} \tag{4.3.31}$$

where $\tilde{f}$ is a constant and $C(\rho)$ is,

$$C(\rho) = 0.001667 + \frac{(0.002568 + \alpha r_s + \beta r_s^2)}{(1 + \gamma r_s + \delta r_s^2 + 10^4 \beta r_s^3)} \tag{4.3.32}$$

where α, β, δ, and γ are constants, and r_s is the Wigner-Seitz radius [128],

$$r_s = \left(\frac{3}{4\pi\rho} \right)^{1/3} \tag{4.3.33}$$

And finally E_C^{LSD} is the local spin density approximation given by,

$$E_C^{LSD}[\rho_\sigma(\mathbf{r})] = \int \rho_\sigma \boldsymbol{\epsilon}_c(\rho_\sigma) d^3\mathbf{r} \tag{4.3.34}$$

where $\epsilon_c(\rho_\sigma)$ is the correlation energy per particle in the uniform electron gas. This value is determined by a parametrization procedure [127].

It is possible to specify several convergence parameters in the program. Convergence generally will depend on the difference between successive iterations of both the electron density and the total energy. In StoBe convergence is achieved when three successive iterations all meet the specified criteria. For all calculations the convergence threshold for the energy difference was set to 1×10^{-6}, and the density convergence was set to 2×10^{-6} — with a couple of calculations requiring this value to be relaxed to 2×10^{-5} to achieve convergence. The order in which the calculations are done, and the steps that are involved are:

1. The pentacene molecule and the location(s) of the Mn atom(s) are first drawn using a free software tool from Accelrys called DS Visualizer 1.7. A *pdb* (Protein Data Bank) structure file is saved as output and the *xyz* coordinates used as input for StoBe. The *xyz* coordinates for all the pentacene structures used are given in Appendix A with a listing of the input files for StoBe.

2. The first step in StoBe is to perform a geometry optimization on the molecule.

3. Next a DOS calculation is done. From the output one can determine the KS-orbital that the half-filled core hole will be assigned to for the subsequent XAS calculation.

4. For an XAS calculation the fractional occupation will need to be assigned to every non-equivalent atom in the molecule. For pentacene this translates into 22 calculations that need to be done to account for the 22 carbon atoms.

5. The final step is to broaden the oscillator strengths of each of the 22 carbon transitions and sum them together, average and then plot the resulting spectrum.

To compare the calculated spectra with experiments two further steps are needed. Since relativistic effects for the IP are not accounted for, shifting the carbon spectra by 0.2 eV is needed to generate absolute energies [129]. For all the spectra presented here, it was also necessary to shift the energy scale by approximately -2 eV to account for the discrepancy between comparing "gas-phase" calculations with the thin-film phase of pentacene. The prominent π^* (unoccupied π orbital) peak found in the experimental carbon spectra was used as the alignment point of the calculated spectra. For the display of XA spectra the oscillator strengths are convoluted with gaussian functions with varying FWHM values. For all the XA spectra of carbon the broadening was set to 0.7 eV for the energy range of 282–293 eV (to approximately match the IP). To account for the increase in lifetime broadening above the IP, the FWHM value is then linearly increased to 4.5 eV between the range of 293–300, and stays at a constant 4.5 eV FWHM from 300–330 eV. This broadening scheme is arbitrary, and is used to more closely match experimental spectra [130].

Chapter 5

Results

5.1 Bond Lengths

The first step toward comparison of theory and experiment involves looking at the correspondence between the experimentally determined structure — using X-ray measurements [131, 132] — and computed geometry optimizations using DFT. The StoBe geometry optimization for the pentacene molecule gives the results shown in figure 5.1 below.

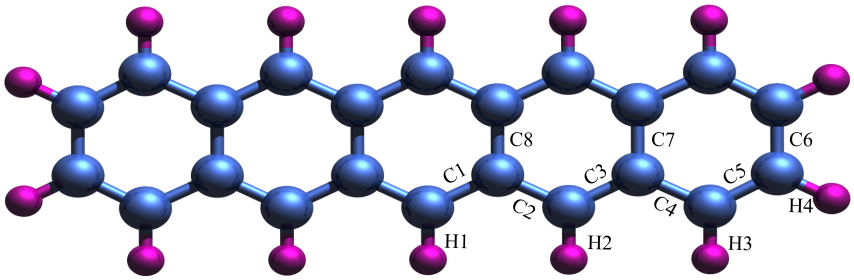

Figure 5.1: StoBe optimized isolated pentacene molecule. Corresponding bond lengths are given in table 5.1 according to the labels in the figure. The missing labels follow from the D_{2h} symmetry of the molecule [133].

Table 5.1 shows two StoBe results in comparison to other computational and experimental results. The *X-ray diffraction* (XRD) results of Campbell *et al.* used Cu $K\alpha$ radiation and recorded on Weissenberg film [131]. These results are for molecular crystals of pentacene in comparison to a single isolated molecule, but the values are quite close due to the weak intermolecular forces in the crystal. The results

Table 5.1: Calculated bond lengths (Å) in comparison with experiment.

	X-ray	**DFT**			
Bond	Campbell [131]	Endres [134]	Lee [135]	StoBe 1	StoBe 2
C1	1.439	1.41	1.393	1.413	1.408
C2	1.380	1.42	1.398	1.423	1.418
C3	1.358	1.40	1.385	1.401	1.396
C4	1.440	1.43	1.412	1.442	1.437
C5	1.357	1.38	1.364	1.378	1.373
C6	1.382	1.43	1.415	1.440	1.434
C7	1.424	1.46	1.436	1.467	1.461
C8	1.433	1.46	1.442	1.469	1.464
H1	N/A	1.10	1.088	1.095	1.095
H2	“	1.10	1.089	1.096	1.095
H3	“	1.10	1.089	1.094	1.095
H4	“	1.10	1.087	1.094	1.094

given by Endres *et al.*[134], and Lee *et al.*[135], were obtained using alternative DFT-based programs.

The StoBe geometry optimization procedure works by moving atoms in the direction of forces until one reaches the convergence thresholds specified. Essentially it makes use of the Hellman-Feynman theorem as given in the equation below:

$$\frac{dE}{d\mathbf{r}} = \left\langle \psi(\mathbf{r}) \left| \frac{dH}{d\mathbf{r}} \right| \psi(\mathbf{r}) \right\rangle \tag{5.1.1}$$

Equation (5.1.1) shows the relationship between the derivative of the total energy with respect to the external potential generated from the electrons. Appendix A provides a reference of the atomic co-ordinates used for all the StoBe calculations done.

The default energy gradient threshold for StoBe is 1.0×10^{-4} $a.u.$, which is the value used for the StoBe #1 column (where 1 $a.u.$ for energy density is equal to 1 $Hartree/Bohr^3$ or 183.633252 $eV/\text{Å}^3$). The StoBe #2 geometry optimization used stricter convergence thresholds (energy gradient set to 1.0×10^{-5} $a.u.$) and also used the Versluis correction to account for the error introduced by numerically determining the exchange-correlation contribution to the energy gradient [136]. This method is useful for organic systems and gives slightly more accurate results at the expense of computation time [116]. The z-coordinates for all the atoms in the optimized molecule were essentially at $z = 0$ — in agreement with experimental findings of oligoacenes being planar molecules [132]. The alternating long and short C bond lengths seen in table 5.1 show agreement with pentacene being labelled as a conjugated molecule.

The XRD data from our collaborators in Korea indicate that the Mn dopants do not degrade the molecular crystal structure of pentacene. Figure 5.2 shows this XRD data and the crystallinity of the samples is clearly seen by the sharp diffraction peaks in the doped samples. The top graph shows a linear intensity scale, while the bottom graph shows the same data on a logarithmic scale, allowing for a more detailed comparison of the samples. It is reasonable to expect that the crystal structure is kept intact as there is a low dopant concentration — 4% Mn translates to ∼1.1 Mn atoms per pentacene molecule and 8% Mn results in ∼1.4 Mn atoms per molecule. This expectation is based on having the Mn atoms occupy interstitial sites in the pentacene crystal structure. The measured D-spacing for the thin film was 15.48 Å for pure pentacene and 15.50 Å for the manganese doped samples.

One of the ongoing challenges with organic semiconductors is finding ways of doping the material without degrading its structural properties [94]. If a material has promising electrical characteristics but is structurally unstable after doping (which is needed to fine-tune the properties), then its suitability for applications is significantly reduced. Our results introducing transition-metal atoms into pentacene, and having the material maintain its original crystal structure, is key for further development of practical uses of this material combination.

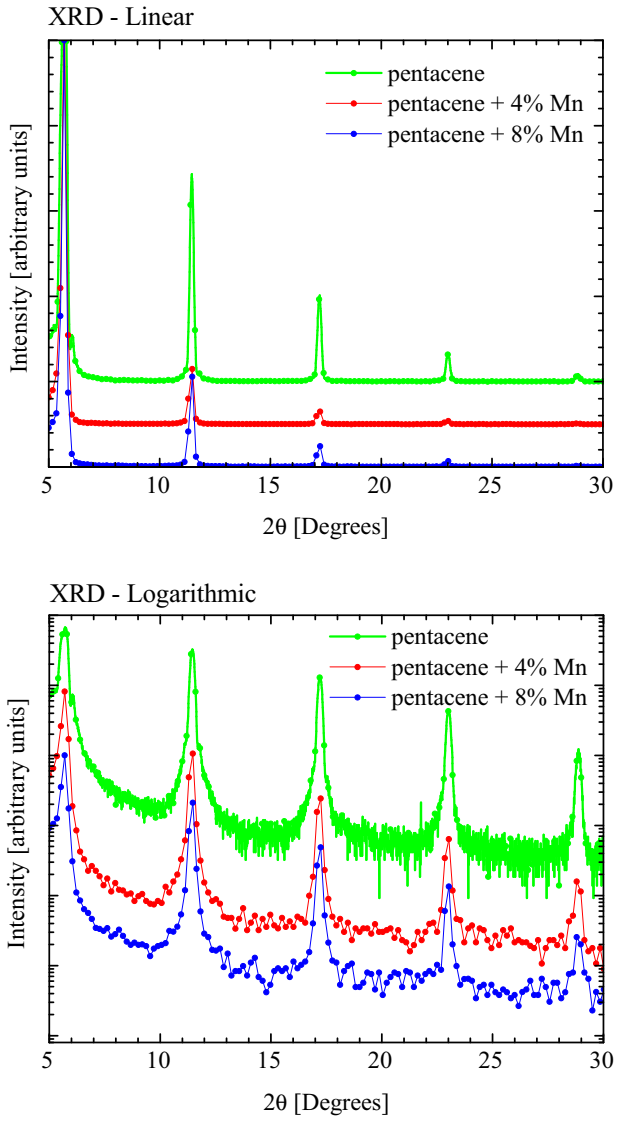

Figure 5.2: X-ray diffraction results showing the same D-spacing for Mn-doped pentacene thin-films as for un-doped pentacene samples.

StoBe calculations which included Mn dopants could be done in two ways. The pentacene molecule and the Mn atoms could be subjected to an overall geometry optimization allowing all atoms to move around, or the alternative way would be to only let the Mn atoms move. Both methods were used depending on the situation as some calculations would not converge to reasonable values unless certain constraints were relaxed. The calculations only allowing the Mn atoms to move used the relaxed (geometry optimized) pentacene structure (StoBe #2) defined in table 5.1.

5.2 Density of States

5.2.1 Pentacene DOS

Calculating the *density of electronic states* (DOS) is useful in interpreting results from XAS measurements and calculations. It can provide an overview of the relative energy levels of the molecular orbitals pictorially through plotting charge density isosurfaces. StoBe was also used to calculate these values, with the isosurface pictures generated from the StoBe output using the MOLEKEL molecular visualization program [137].

DOS energy levels have the benefit of not being affected by a core hole (as there is not one present in the calculations) and the subsequent difficulties that result in trying to model the core hole. The calculations and results are considerably quicker to perform and analyse without a core hole being present. The DOS results presented are shown on a binding energy scale, with 0 eV taken to be the ionization potential. The charge density isosurfaces are plotted using an isosurface value of 0.02 $e/a.u.^3$ The electron density plots show the results of squaring the wavefunction ψ_i. The two different colours in the plots (blue and olive) correspond to positive and negative values that are input into the wavefunction before it is squared, and have no intrinsic physical meaning. They are used simply to aid in visualization of the orbitals.

The *total DOS* (TDOS) along with the *partial* or *projected DOS* (PDOS) is able to clarify what atoms or MOs are involved with the HOMO and LUMO states of the molecule. Figure 5.3 shows the TDOS for an isolated pentacene molecule. Also shown in the figure, below the TDOS, is the p_x, p_y, and p_z PDOS for all 22 carbon atoms in the molecule. One can clearly see that the p_z orbitals are the main contributors to the HOMO-LUMO levels due to their delocalized nature. Figure 5.4 shows the PDOS for each carbon atom in the molecule. A vertical offset was added to each spectrum for clarity.

It is easy to see from the site-resolved PDOS that the outer carbon atoms are responsible for the HOMO and LUMO levels as they possess extra electrons occupying

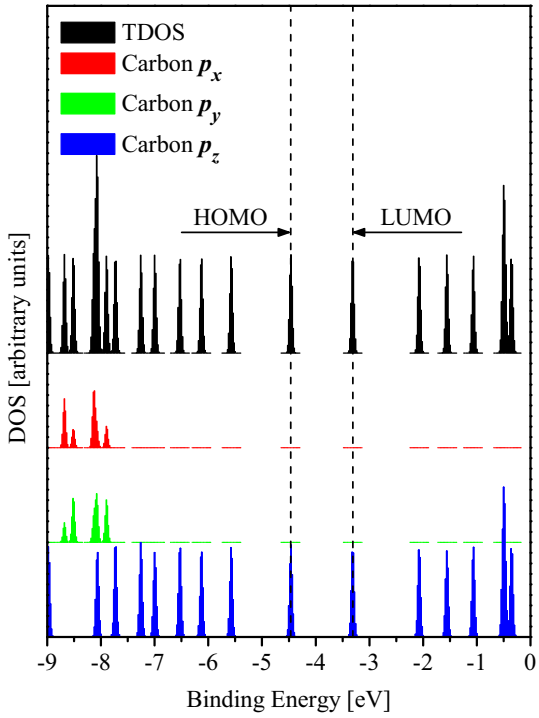

Figure 5.3: Total DOS of pentacene, and the corresponding p_x, p_y, and p_z partial DOS for the carbon atoms in pentacene.

the p_z orbitals. We can see that if the Mn atoms hybridize with these particular carbon MOs that it will affect the HOMO-LUMO gap and subsequently the electronic properties of the OFETs. To investigate this possibility figure 5.5 shows locations that Mn atoms were placed to see how the transition metal atom might affect the HOMO-LUMO gap of the isolated pentacene molecule. The positions shown are the result of calculations that converged. The geometry optimization runs for positions A, B, and C resulted in a final geometry very similar to the positions already shown in figure 5.5. Position D was an energetically unstable configuration and the Mn atom ended up close to position C after the geometry optimization. The results presented here will be with the Mn atom in position C as it provided the best agreement with experimental results.

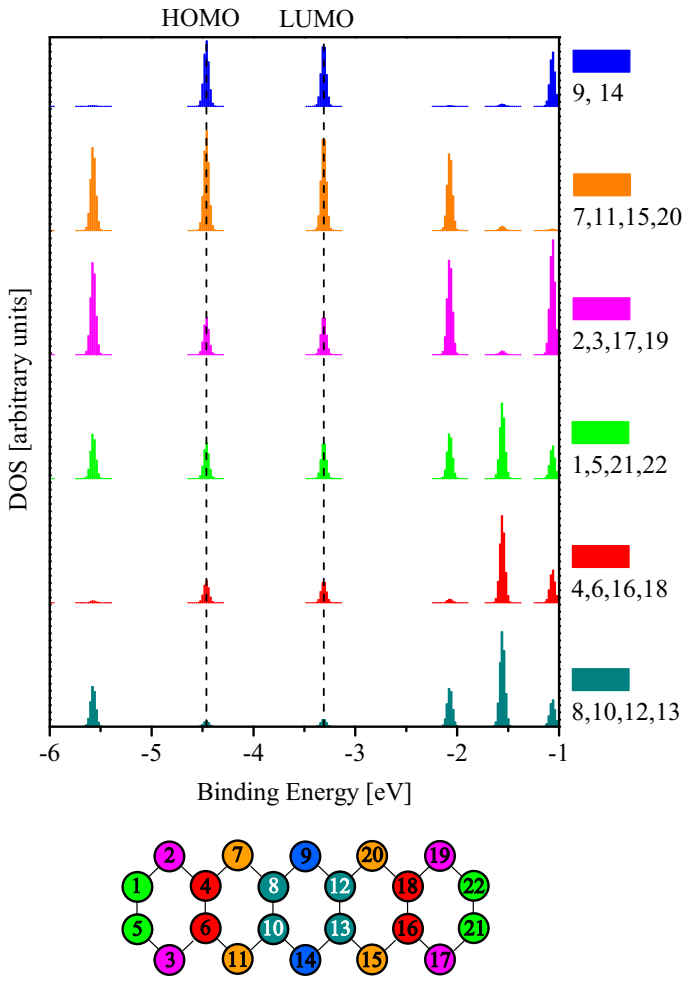

Figure 5.4: Partial DOS of symmetric carbon atoms in pentacene.

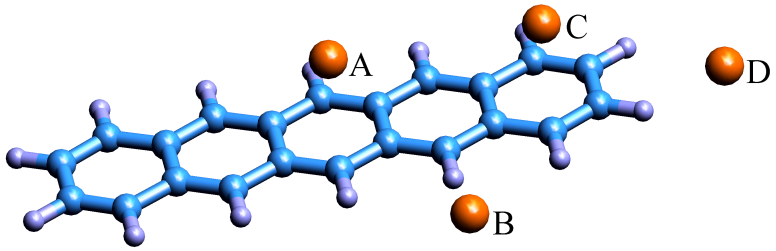

Figure 5.5: Location of Mn atoms used in DFT calculations

5.2.2 HOMO-LUMO Energy Gap

Our calculated energy gap (ΔE) between the HOMO and LUMO level is 1.18 eV for an isolated pentacene molecule. This is about 80% less than the experimental values found for measurements done on the gas phase — which give ΔE=5.22 eV [138, 139]. This is a well known deficiency with DFT-based approaches, and is partly due to the fact that the exchange-correlation functional (as a function of electron density) has a discontinuity that is not accounted for, and also possesses the wrong asymptotic behaviour at large distances [140, 141]. This value however is consistent with other values found using DFT. Lee *et al.* found ΔE=1.08 eV [135], and Potera *et al.* ΔE=1.13 eV [133]. For pentacene molecular crystals the computed values for the band-gaps have been found to be 0.97 eV and 0.98 eV [142], 0.58 eV [143], and 0.95 eV [134], all taken at the Γ point for the crystal. Computed values are consistently lower than experimental values [142]. The experimental value has been determined to be 1.82 eV [144].

5.2.3 DOS of Mn-doped Pentacene

The TDOS and PDOS of pentacene is shown in figure 5.6, with the corresponding TDOS and PDOS of the manganese doped sample compared beside it. It is easy to see from figure 5.6 that the Mn atom has a strong contribution to the DOS around the HOMO/LUMO levels of the system. The HOMO shift that results from the addition of manganese is $+0.7$ eV, and the LUMO shift becomes -0.2 eV. This changes the energy spacing between the HOMO and LUMO for the Mn-doped sample to 0.25 eV, versus the much larger 1.15 eV for pentacene. The small gap between the HOMO and LUMO levels indicates that the Mn atom hybridizes with the carbon atoms in this energy range, promoting the material to a semi-metallic state [145]. This result combined with the greater PDOS of Mn present in the LUMO versus the HOMO, indicates that the Mn dopants will act as donor impurities, versus the more commonly found acceptor impurities in organic materials. This hypothesis was confirmed by performing current versus voltage measurements of the Mn-doped

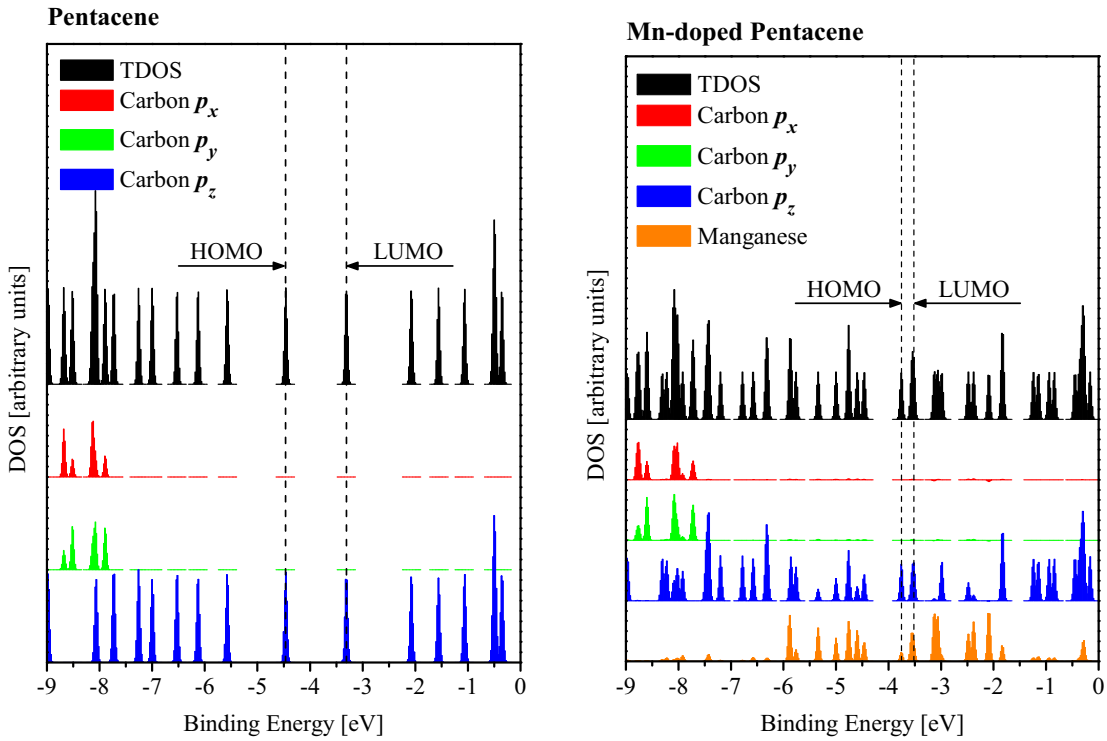

Figure 5.6: The TDOS and PDOS of pentacene and Mn-doped pentacene compared.

OFETs and comparing them to undoped samples. These measurements were done by our collaborators at Yonsei University, in Seoul, South Korea.

Figure 5.7 shows a pictorial view of the previous result showing the extent that the HOMO and LUMO orbitals of pentacene change with the addition of manganese. This pictorial view shows more clearly the hybridization occurring between the Mn atom and the carbon atoms. These DOS results further the idea that the Mn dopants are actively involved in the charge transfer occurring in the organic devices. To verify this idea, experimental XAS findings are compared with theoretical StoBe results in the next section.

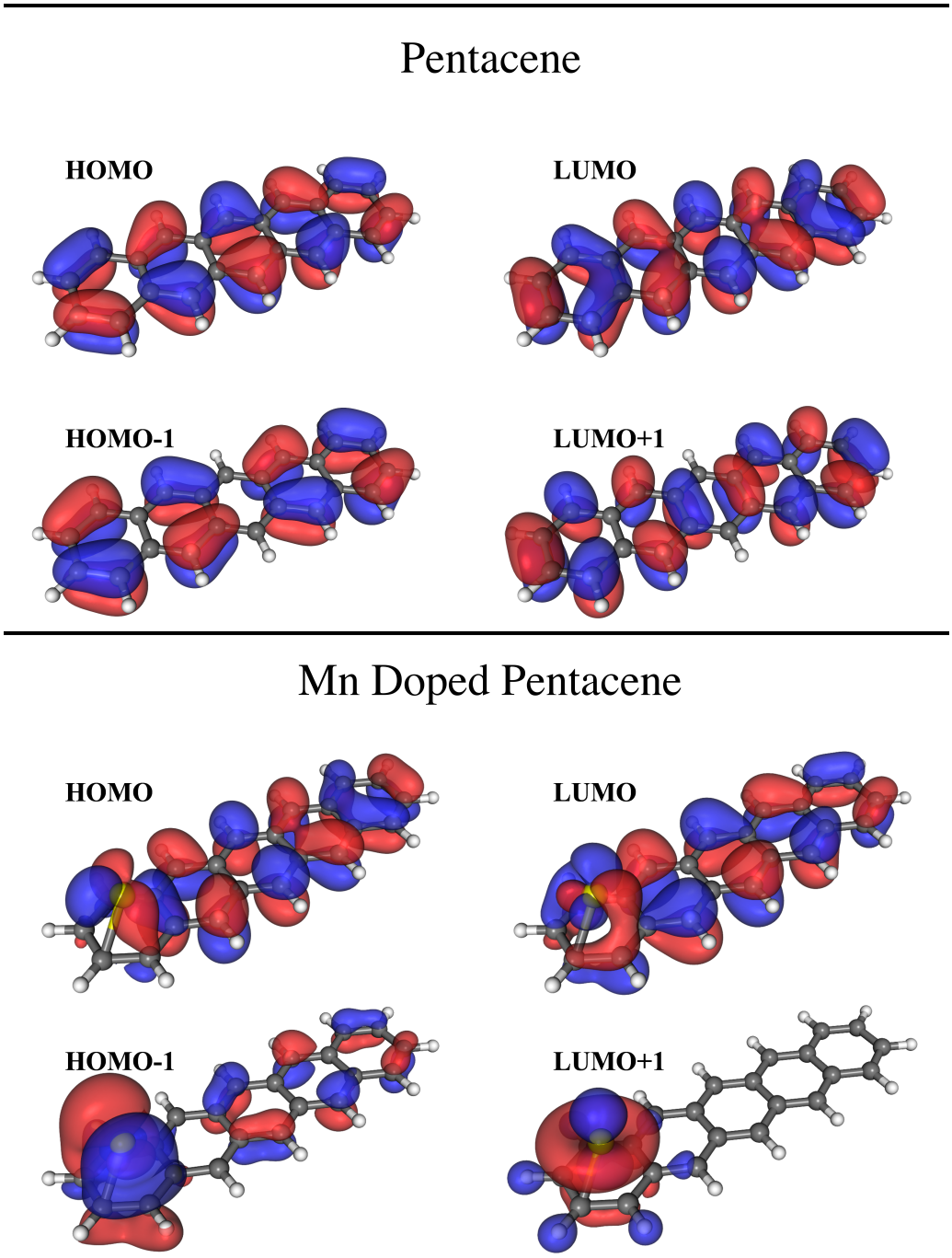

Figure 5.7: The charge density isosurfaces for pentacene are shown on the top and for Mn-doped pentacene on the bottom.

5.3 X-ray Absorption Spectroscopy

All of the X-ray absorption spectra shown have been aligned to a reference sample with a known energy value. For the carbon $1s$ edge, *highly oriented pyrolytic graphite* (HOPG) was used, with the LUMO peak occurring at 285.5 eV. The resolving power ($E/\Delta E$) of the beamline at the ALS for carbon XAS is approximately 5000. All absorption measurements presented were done in TEY mode.

One of the key difficulties in modeling materials with DFT techniques is the inherent limit in the number of atoms that can be modeled. This creates the challenge, that is present in this work, of comparing calculations that are based on an isolated pentacene molecule, with experimental measurements that are done on the crystalline phase of the material. There have been comparisons made with experimental measurements of the gas-phase of pentacene with DFT calculations. This will be looked at below as it provides an overview of the issues involved with comparing DFT calculations with XAS measurements.

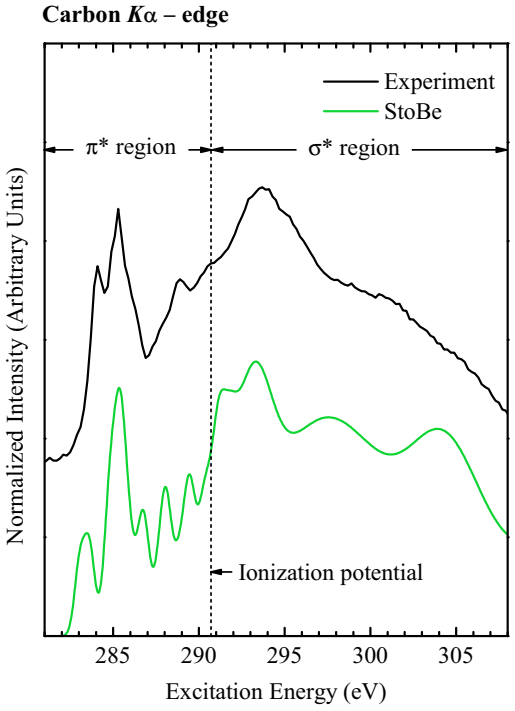

Figure 5.8: XA spectrum for the carbon K-edge for the thin-film phase of pentacene compared with the StoBe calculated result.

Figure 5.8 shows the calculated StoBe XA spectrum for an isolated pentacene molecule compared with the experimental spectrum for the solid thin-film phase of pentacene. The spectra are vertically offset for clarity, a linear background is subtracted, and the intensity normalized at 285.5 eV. The π^* and σ^* regions correspond to unoccupied MOs that possess π- and σ-like symmetry. The star symbol (*) is used to represent an excited orbital, or one that is unoccupied in the ground state. The calculated values have been shifted with respect to the calibrated experimental spectrum by -1.8 eV. A small energy shift is common with DFT-based approaches to modelling experimental spectra and can be attributed to deficiencies with the exchange and correlation functionals used [146]. The agreement between the experimental and theoretical spectra is acceptable, with the main peaks appearing at the correct locations. The agreement between the intensity ratios could be improved by varying the broadening and weighting of each individual carbon atom. The focus of this research is on the modification of the HOMO and LUMO levels of pentacene and therefore improving the agreement between the higher excited orbitals is not needed.

Figure 5.9 is from a paper that performed NEXAFS measurements on the gas-phase of pentacene [147]. The "C 1s edge" label in the above figure is very close to

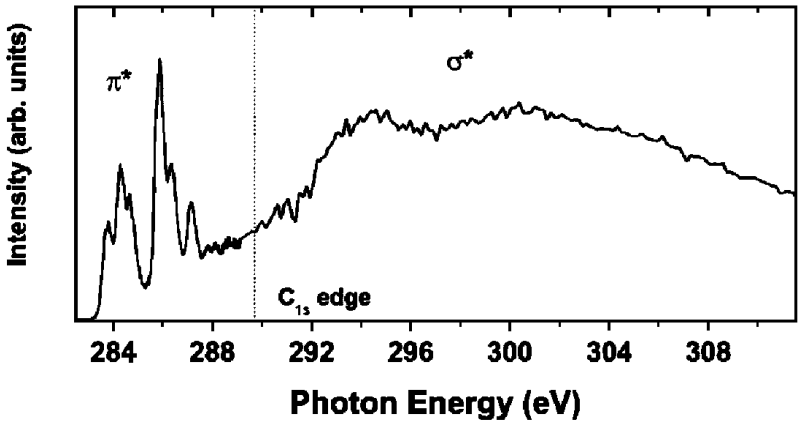

Figure 5.9: XA spectrum of the gas-phase of pentacene. Fig. from ref. [147].

the ionization potential (IP) found in our calculations, as shown in figure 5.8. The IP

for the experimental gas-phase is $\sim 0.5\ eV$ lower than our value for the experimental thin-film phase. This can be attributed to the difference in phases of the two systems. On a qualitative level the fine structure seen in figure 5.9, more closely resembles the theoretical spectra computed with StoBe. This is to be expected as the calculations are modelling an isolated molecule.

The peaks below the IP in figure 5.8 can be further resolved into various MOs. Figure 5.10 shows the breakdown of the pentacene XA spectrum into the contribu-

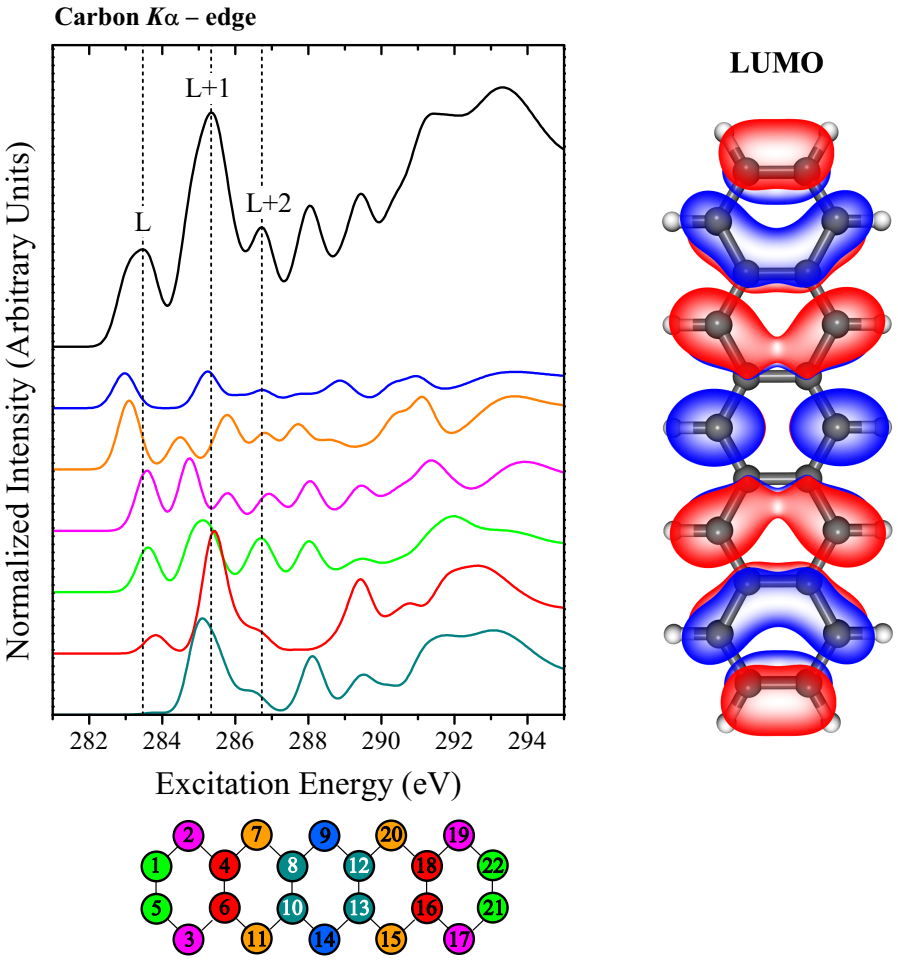

Figure 5.10: Atom-resolved breakdown of the pentacene XA spectrum. The DOS isosurface is shown for the LUMO on the right hand side.

tions arising from the inequivalent carbon atoms. The different colours in the figure correspond to groups of atoms possessing the same symmetry in the molecule. Also

labelled in the figure are the tentative assignments of the LUMO (L), LUMO+1 (L+1), and LUMO+2 (L+2) molecular orbitals.

From figure 5.10 it can be seen again that the outer carbon atoms are responsible for the LUMO level, with the inner atoms contributing little to it. The DOS isosurface for the LUMO is also shown on the right side of the figure. It can be seen that the LUMO isosurface agrees qualitatively with the XA LUMO peak. The XA spectrum shows almost all carbon atoms contributing — except atoms 8, 10, 12, and 13 — which are also the partially exposed atoms seen in the middle of the LUMO DOS isosurface of pentacene.

The measured XA spectra for the Mn-doped pentacene samples are shown in figure 5.11. The pentacene samples were doped with both four and eight percent manganese, although the difference between the two doping concentrations is not particularly noticeable in the XA spectra. The key point to take from the figure is

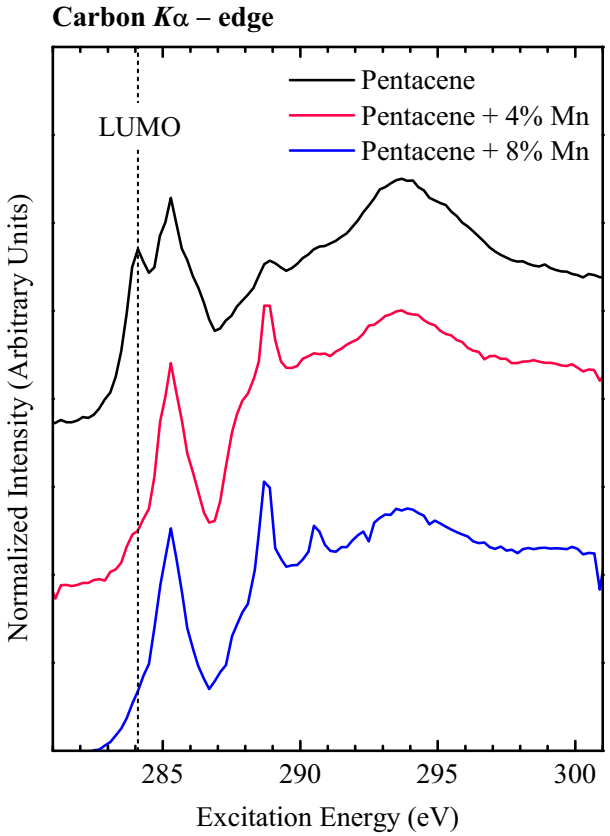

Figure 5.11: The experimental XA spectra showing the decrease in the π^* peak (LUMO) due to the Mn dopant atoms.

that the π^* LUMO peak decreases with the addition of Mn dopants. The hypothesis is that by adding metal dopant atoms the HOMO/LUMO levels of pentacene are modified. The Mn dopants have energetically similar orbitals with pentacene allowing for hybridization of the π-MOs of carbon with the p_z-orbitals of Mn. This can be attributed to charge transfer from the metal atoms to the organic semiconductor, which can be seen in the charge density isosurfaces of the Mn-doped sample (Fig. 5.7) [148].

Figure 5.12 shows the StoBe calculated XA spectra for plain pentacene, and Mn-doped pentacene. It also clearly shows a decrease in the LUMO peak with the

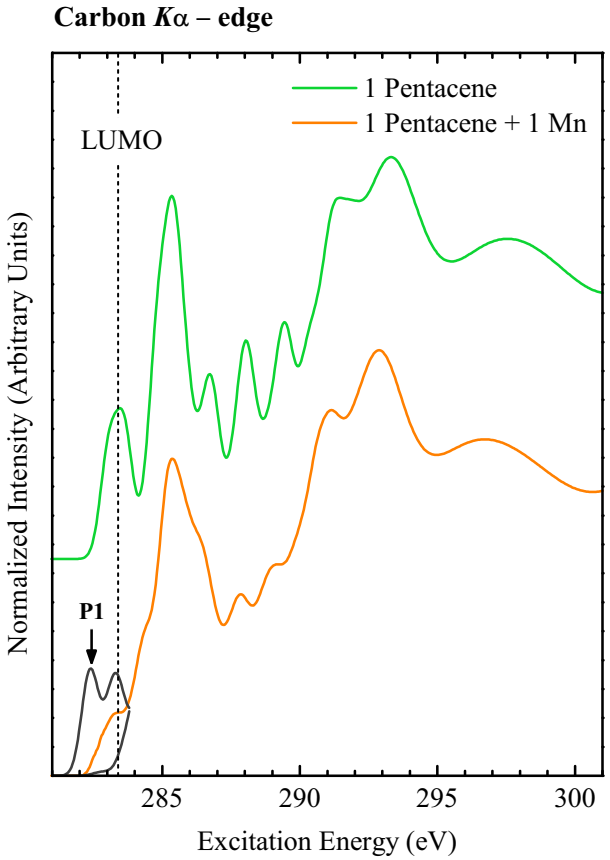

Figure 5.12: The StoBe XA spectra also shows a corresponding decrease in the π^* peak. The peak labelled "P1" is the phantom peak that is removed in calculating the final spectrum.

addition of the Mn atom. DFT is known to have problems when modelling open spin systems. This is the exact situation that occurs when adding one Mn atom to pentacene, as the atomic number for Mn is 25. This results in an unpaired valence

electron for the Mn atom in the doped pentacene system. There are no special computational routines in StoBe to account for this issue [116]. As a result, the raw XA spectrum will have a peak (labelled "P1"), at a lower energy than the LUMO, that arises from having an unoccupied beta orbital in the ground state. The two black lines are the raw calculated values for the alpha and beta orbitals. Once the P1 peak has been subtracted out, and the alpha and beta orbital contributions averaged, one is left with the orange line shown. In a closed spin system, the StoBe calculated values for alpha and beta orbitals are equivalent, and it suffices to only use the alpha orbital values. It is clear from these figures that both experimental and theoretical results show a decrease in the LUMO peak when Mn is present.

Figure 5.13 extracts the Mn-doped data from the two previous figures (5.11 and 5.12) and compares the experimental results with the StoBe calculated spectrum. For the two experimental peaks (red and blue), the feature at $\sim 289\ eV$ contrasts

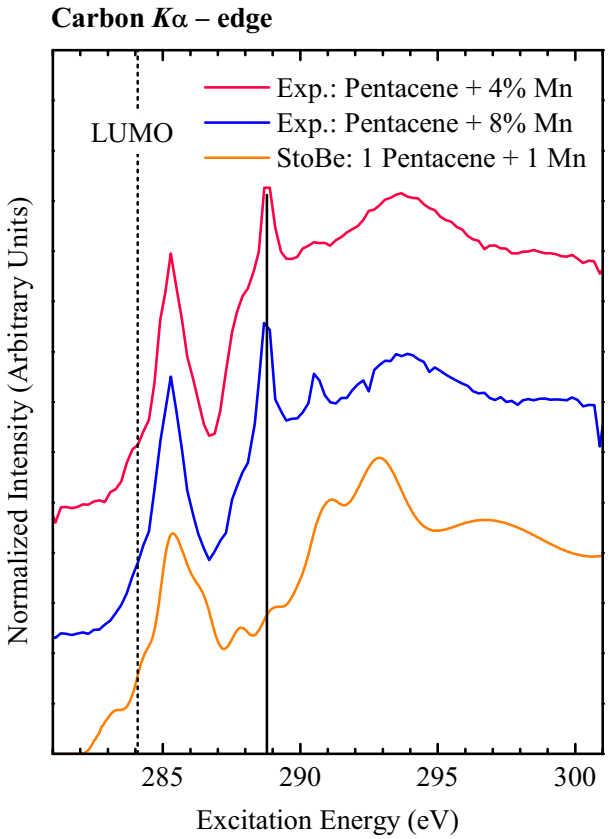

Figure 5.13: The experimental XA spectra measured at the ALS compared to the calculated XA spectrum done with StoBe.

with the StoBe calculated result (orange). The possible reasons for this are unclear. The feature is similar in shape and energy to a carbon/oxygen double bond. This would only arise if there was contamination in the samples, as oxygen is not part of the molecular structure of pentacene. If oxygen was present in the samples it would have affected the quality of the XRD results, but that was not seen to be the case. Another possibility is that the samples are exhibiting Rydberg states; although this also is unlikely, as Rydberg states are traditionally only seen in gas samples and are generally suppressed in the condensed phase [149]. The final possibility is that the exchange and correlation potentials that were used are not sufficiently accurate to deal with these higher excited states. Since we are primarily concerned with the HOMO and LUMO levels, it is still possible to have confidence in the qualitative agreement of the LUMO peak in the experimental and theoretical spectra — as the feature at 289 eV is ~ 5 eV higher in energy than the LUMO at 284 eV.

The decrease in the LUMO peak can be attributed to the Mn atoms taking part in the conduction mechanism of pentacene. In this model the excited electron moves from a delocalized π orbital of carbon to an intermediate Mn orbital, and then on to the next pentacene molecule. In essence this is a hopping conduction mechanism with the Mn atoms taking part in transferring the electrons along the pentacene molecules. This is where the possibility for spintronic applications comes in. If one is able to manipulate the Mn atoms, either through magnetic or electrical means, into a specific spin orientation, it would be possible to inhibit the flow of electrons possessing the wrong spin orientation.

Chapter 6

Conclusions and Recommendations

6.1 Conclusions

The conclusions drawn from this research are summarized below.

1. The geometry optimization of the pentacene molecule, performed using the DFT program StoBe, is consistent with other research that used both different computational programs and theoretical methods.

2. Both the experimental and StoBe XAS results agree, as far as having the LUMO peak height decrease in Mn-doped pentacene, in comparison with plain pentacene.

3. The DOS results indicate that the Mn dopants act as electron donors. This result is consistent with the device characteristics found by our collaborators at Yonsei University in Seoul, South Korea.

The end goal of this research is to find unique structural materials (i.e. organics) that could be used to bring about spintronic applications and/or create computational devices. This research was able to develop and verify a basic model for the conduction mechanism in Mn-doped pentacene OFETs. The premise is that Mn atoms act as electron donors in the organic heterostructure, thereby hybridizing with the delocalized p_z-orbitals of carbon. These hybridized molecular orbitals create a "conduit" for electrons to travel on as they move from pentacene molecule to pentacene molecule in the crystal. The evidence for this model is based on the results from the X-ray absorption measurements and the corresponding DFT calculations.

If this initial research for Mn-doped pentacene holds true, then it may be possible to develop unique organic devices that are able to carry out computational tasks, and also be used as non-volatile storage — concurrently. It depends on whether a suitable method can be found to control the spin orientation of the Mn atoms. If that is successful then these and other applications can also be envisioned, such as organic spin valves (i.e. GMR read heads).

6.2 Recommendations

It is possible to perform theoretical calculations that take into account the crystal structure of pentacene. Two common programs that have been used for molecular crystals are WIEN2k [150] and VASP [151]. The following references have used these programs on pentacene (and other organic materials) to determine primarily energy bandgaps and bandwidths [60, 62, 142, 152–158]. The benefit of doing such calculations would be to determine the extent of the intermolecular interactions due to the Mn dopant atoms. Being able to elucidate how the Mn atoms interact with one another would enable the tailoring of the carrier mobilities. This would be beneficial as organic semiconductors exhibit highly anisotropic charge transport due to this intermolecular interaction [94].

Further calculations could also be done with StoBe to see if other transition metals have a similar effect on the XAS and DOS results. Additional experimental and theoretical work with other similar organic materials, such as anthracene, could also prove enlightening.

References

[1] I. Zutic, J. Fabian, and S.D. Sarma. Spintronics: Fundamentals and applications. *Rev. Mod. Phys.*, 76(2):323–388, 2004.

[2] S.A. Wolf, A.Y. Chtchelkanova, and D.M. Treger. Spintronics - a retrospective and perspective. *IBM J. Res. Dev.*, 50:101–110, 2006.

[3] D.D. Awschalom, M.E. Flatte, and N. Samarth. Spintronics. *Sci. Amer.*, 286: 52–59, 2002.

[4] A. Barenco, A. Ekert, A. Sanpera, and C. Machiavello. A short introduction to quantum computation., 1996. URL `http://cam.qubit.org/articles/intros/comp.php`. Accessed on: Apr. 12, 2008.

[5] D-wave: The quantum computing company. URL `http://www.dwavesys.com/`. Accessed on: Apr. 12, 2008.

[6] G. Binasch, P. Grünberg, F. Saurenbach, and W. Zinn. Enhanced magnetoresistance in layered magnetic structures with antiferromagnetic interlayer exchange. *Phys. Rev. B*, 39(7):4828–4830, 1989.

[7] M.N. Baibich, J.M. Broto, A. Fert, F. Nguyen van Dau, F. Petroff, P. Eitenne, G. Creuzet, A. Friederich, and J. Chazelas. Giant Magnetoresistance of (001)Fe/(001)Cr Magnetic Superlattices. *Phys. Rev. Lett.*, 61(21):2472–2475, 1988.

[8] IBM. The giant magnetoresistive head: A giant leap for ibm research. URL `http://www.research.ibm.com/research/gmr.html`. Accessed on: Apr. 12, 2008.

[9] W.J. Gallagher and S.S.P. Parkin. Development of the magnetic tunnel junction MRAM at IBM: From first junctions to a 16 Mb MRAM demonstrator chip. *IBM J. Res. Dev.*, 50:1, 2006.

[10] S.D. Bader. Colloquium: Opportunities in nanomagnetism. *Rev. Mod. Phys.*, 78(1):1–15, 2006.

[11] A.H. MacDonald, P. Schiffer, and N. Samarth. Ferromagnetic semiconductors: moving beyond (Ga,Mn)As. *Nat. Mater.*, 4(3):195–202, 2005.

[12] H. Ohno. Making Nonmagnetic Semiconductors Ferromagnetic. *Science*, 281 (5379):951–956, 1998.

[13] S. Pearton. Magnetic semiconductors: Silicon-based spintronics. *Nat. Mater.*, 3(4):203–204, 2004.

[14] D.B. Mitzi, K. Chondroudis, and C.R. Kagan. Organic-inorganic electronics. *IBM J. Res. Dev.*, 1:29–45, 2001.

[15] P. Sharma. Physics: How to create a spin current. *Science*, 307(5709):531–533, 2005.

[16] V.A. Ivanov, T.G. Aminov, V.M. Novotortsev, and V.T. Kalinnikov. Spintronics and spintronics materials. *Russ. Chem. Bull., Intl. Ed.*, 53(11):2357–2405, 2004.

[17] S.A. Wolf, D.D. Awschalom, R.A. Buhrman, J.M. Daughton, S. von Molnar, M.L. Roukes, A.Y. Chtchelkanova, and D.M. Treger. Spintronics: A spin-based electronics vision for the future. *Science*, 294(5546):1488–1495, 2001.

[18] B.A. Bernevig and S. Zhang. Toward dissipationless spin transport in semiconductors. *IBM J. Res. Dev.*, 50:141–148, 2006.

[19] A.R. Rocha, V.M. Garcia-suarez, S.W. Bailey, C.J. Lambert, J. Ferrer, and S. Sanvito. Towards molecular spintronics. *Nat. Mater.*, 4(4):335–339, 2005.

[20] E.W. Weisstein. Quaternary - from mathworld–a wolfram web resource, 2002. URL `http://mathworld.wolfram.com/Quaternary.html`. Accessed on: Apr. 12, 2008.

[21] P. Sharma and C. Chamon. Quantum Pump for Spin and Charge Transport in a Luttinger Liquid. *Phys. Rev. Lett.*, 87(9):096401–, 2001.

[22] J. Stöhr. *NEXAFS Spectroscopy*. Springer-Verlag, 1992.

[23] B.A. Bolto, R. McNeill, and D.E. Weiss. Electronic Conduction in Polymers. I. The Chemical Structure of Polypyrrole. *Austr. J. Chem.*, 16:1090–1103, 1963.

[24] C.K. Chiang, C.R. Fincher, Y.W. Park, A.J. Heeger, H. Shirakawa, E.J. Louis, S.C. Gau, and A.G. MacDiarmid. Electrical conductivity in doped polyacetylene. *Phys. Rev. Lett.*, 39(17):1098–1101, 1977.

[25] P. Proctor. Who discovered the first high-conductivity organic polymer?, 2006. URL `http://www.drproctor.com/os/whine.htm`. Accessed on: Apr. 12, 2008.

[26] J.M. Shaw and P.F. Seidler. Organic electronics: Introduction. *IBM J. Res. Dev.*, 45:3–9, 2001.

[27] M.E. Gershenson, V. Podzorov, and A.F. Morpurgo. Colloquium: Electronic transport in single-crystal organic transistors. *Rev. Mod. Phys.*, 78(3):973–17, 2006.

[28] M.V. Tiba. *Organo-metallic structures for spintronic applications*. PhD thesis, Eindhoven University of Technology, 2005.

[29] I. Zutic, J. Fabian, and S.C. Erwin. Bipolar spintronics: Fundamentals and applications. *IBM J. Res. Dev.*, 50:121–139, 2006.

[30] C.D. Dimitrakopoulos and D.J. Mascaro. Organic thin-film transistors: A review of recent advances. *IBM J. Res. Dev.*, 45:11–26, 2001.

[31] R.M. Ramanathan and R. Willoner. Silicon innovation: Leaping from 90 nm to 65 nm. *Technology@Intel Mag.*, March:1–9, 2006.

[32] Y.-Y. Lin, D.J. Gundlach, S.F. Nelson, and T.N. Jackson. Stacked pentacene layer organic thin-film transistors with improved characteristics. *Electr. Dev. Lett., IEEE*, 18(12):606–608, 1997.

[33] O.D. Jurchescu, M. Popinciuc, B.J. van Wees, and T.T.M. Palstra. Interface-controlled, high-mobility organic transistors. *Adv. Mat.*, 19(5):688–692, 2007.

[34] M. Unge. *Molecular Electronics: A Theoretical Study of Electronic Structure of Bulk and Interfaces*. PhD thesis, Linkopings Universitet, 2005.

[35] G. Horowitz, R. Hajlaoui, R. Bourguiga, and M. Hajlaoui. Theory of the organic field-effect transistor. *Synth. Met.*, 101(1-3):401–404, 1999.

[36] M. Razeghi. *Fundamentals of Solid State Engineering*. Kluwer Academic Publishers, 2002.

[37] A. Facchetti. Semiconductors for organic transistors. *Mat. Today*, 10(3):28–37, 2007.

[38] J.H. Seo, D.S. Park, S.W. Cho, C.Y. Kim, W.C. Jang, C.N. Whang, K.-H. Yoo, G.S. Chang, T. Pedersen, A. Moewes, K.H. Chae, and S.J. Cho. Buffer layer effect on the structural and electrical properties of rubrene-based organic thin-film transistors. *Appl. Phys. Lett.*, 89(16):163505–3, 2006.

[39] A.F. Stassen, R.W.I. de Boer, N.N. Iosad, and A.F. Morpurgo. Influence of the gate dielectric on the mobility of rubrene single-crystal field-effect transistors. *Appl. Phys. Lett.*, 85(17):3899–3901, 2004.

[40] I.H. Campbell, J.D. Kress, R.L. Martin, D.L. Smith, N.N. Barashkov, and J.P. Ferraris. Controlling charge injection in organic electronic devices using self-assembled monolayers. *Appl. Phys. Lett.*, 71(24):3528–3530, 1997.

[41] H.-G. Boyen, P. Ziemann, U. Wiedwald, V. Ivanova, D.M. Kolb, S. Sakong, A. Gross, A. Romanyuk, M. Buttner, and P. Oelhafen. Local density of states effects at the metal-molecule interfaces in a molecular device. *Nat. Mater.*, 5 (5):394–399, 2006.

[42] A. Molinari, I. Gutierrez, I. N. Hulea, S. Russo, and A.F. Morpurgo. Bias-dependent contact resistance in rubrene single-crystal field-effect transistors. *Appl. Phys. Lett.*, 90(21):212103–3, 2007.

[43] S.J. Kang, Y. Yi, C.Y. Kim, C.N. Whang, T.A. Callcott, K. Krochak, A. Moewes, and G.S. Chang. Analysis of octadecyltrichlorosilane treatment of organic thin-film transistors using soft x-ray fluorescence spectroscopy. *Appl. Phys. Lett.*, 86(23):232103–3, 2005.

[44] H. Fukagawa, S. Kera, T. Kataoka, S. Hosoumi, Y. Watanabe, K. Kudo, and N. Ueno. The role of the ionization potential in vacuum-level alignment at organic semiconductor interfaces. *Adv. Mat.*, 19(5):665–668, 2007.

[45] M. Popinciuc, H.T. Jonkman, and B.J. van Wees. Energy level alignment symmetry at Co/pentacene/Co interfaces. *J. Appl. Phys.*, 100(9):093714–8, 2006.

[46] L.-L. Chua, J. Zaumseil, J.-F. Chang, E.C.-W. Ou, P.K.-H. Ho, H. Sirringhaus, and R.H. Friend. General observation of n-type field-effect behaviour in organic semiconductors. *Nature*, 434(7030):194–199, 2005.

[47] A.C. Mayer, A. Kazimirov, and G.G. Malliaras. Dynamics of bimodal growth in pentacene thin films. *Phys. Rev. Lett.*, 97(10):105503–4, 2006.

[48] F. Jiang, Y.X. Zhou, H. Chen, R. Note, H. Mizuseki, and Y. Kawazoe. Self-consistent study of single molecular transistor modulated by transverse field. *J. Chem. Phys.*, 125(8):084710–6, 2006.

[49] C.C. Mattheus. *Polymorphism and electronic properties of pentacene*. PhD thesis, University of Groningen, 2002.

[50] D.V. Lang, X. Chi, T. Siegrist, A.M. Sergent, and A.P. Ramirez. Amorphous-like density of gap states in single-crystal pentacene. *Phys. Rev. Lett.*, 93(8): 086802–4, 2004.

[51] V. Podzorov, E. Menard, J.A. Rogers, and M.E. Gershenson. Hall effect in the accumulation layers on the surface of organic semiconductors. *Phys. Rev. Lett.*, 95(22):226601–4, 2005.

[52] S.R. Forrest. The path to ubiquitous and low-cost organic electronic appliances on plastic. *Nature*, 428(6986):911–918, 2004.

[53] K. Hannewald and P.A. Bobbert. Anisotropy effects in phonon-assisted charge-carrier transport in organic molecular crystals. *Phys. Rev. B*, 69(7):075212–12, 2004.

[54] V. Podzorov, E. Menard, A. Borissov, V. Kiryukhin, J.A. Rogers, and M.E. Gershenson. Intrinsic charge transport on the surface of organic semiconductors. *Phys. Rev. Lett.*, 93(8):086602–4, 2004.

[55] D.M. Larsen and D. Emin. Polaron, October 2007. URL `http://www.accessscience.com/abstract.aspx?id=532700`. Accessed on: Apr. 12, 2008.

[56] M.F. Calhoun, C. Hsieh, and V. Podzorov. Effect of interfacial shallow traps on polaron transport at the surface of organic semiconductors. *Phys. Rev. Lett.*, 98(9):096402–4, 2007.

[57] D.A. da Silva Filho, E.-G. Kim, and J.-L. Brédas. Transport properties in the rubrene crystal: Electronic coupling and vibrational reorganization energy. *Adv. Mat.*, 17(8):1072–1076, 2005.

[58] Y. Sakamoto, T. Suzuki, M. Kobayashi, Y. Gao, Y. Fukai, Y. Inoue, F. Sato, and S. Tokito. Perfluoropentacene: High-performance p-n junctions and complementary circuits with pentacene. *JACS*, 126(26):8138–8140, 2004.

[59] N. Benson, M. Schidleja, C. Melzer, R. Schmechel, and H. von Seggern. Complementary organic field effect transistors by ultraviolet dielectric interface modification. *Appl. Phys. Lett.*, 89(18):182105–3, 2006.

[60] A. Hansson, J. Bohlin, and S. Stafstrom. Structural and electronic transitions in potassium-doped pentacene. *Phys. Rev. B*, 73(18):184114–4, 2006.

[61] M. Cazayous, A. Sacuto, G. Horowitz, Ph. Lang, A. Zimmers, and R.P.S.M. Lobo. Iodine insertion in pentacene thin films investigated by infrared and raman spectroscopy. *Phys. Rev. B*, 70(8):081309–4, 2004.

[62] Y. Shichibu and K. Watanabe. Ab initio study on electronic structures of pentacene molecular crystals with dopants. *Jpn. J. Appl. Phys.*, 42:5472–5476, 2003.

[63] W.J. Yun, J.M. Cho, and J.-K. Lee. Electron spin resonance measurements of iodine-doped pentacene films. *Synth. Met.*, 156(11-13):848–851, 2006.

[64] Y. Matsuo, S. Sasaki, and S. Ikehata. Electric properties on iodine doped pentacene. *Synth. Met.*, 121(1-3):1383–1384, 2001.

[65] Y. Matsuo, S. Sasaki, and S. Ikehata. Magnetic properties in rubidium doped pentacene. *Synth. Met.*, 137(1-3):955–956, 2003.

[66] Y. Matsuo, T. Ijichi, H. Yamada, J. Hatori, and S. Ikehata. Electrical properties and memory effect in the field effect transistor based on organic ferroelectric insulator and pentacene. *Centr. Euro. J. Phys.*, 2(2):357–366, 2004.

[67] Y. Matsuo, S. Sasaki, and S. Ikehata. Stage structure and electrical properties of rubidium-doped pentacene. *Phys. Lett. A*, 321(1):62–66, 2004.

[68] Y. Kaneko, T. Suzuki, Y. Matsuo, and S. Ikehata. Metallic electrical conduction in alkaline metal-doped pentacene. *Synth. Met.*, 154(1-3):177–180, 2005.

[69] T. Minakata, H. Imai, M. Ozaki, and K. Saco. Structural studies on highly ordered and highly conductive thin films of pentacene. *J. Appl. Phys.*, 72(11): 5220–5225, 1992.

[70] T. Minakata, M. Ozaki, and H. Imai. Conducting thin films of pentacene doped with alkaline metals. *J. Appl. Phys.*, 74(2):1079–1082, 1993.

[71] B. Fang, H. Zhou, and I. Honma. Electrochemical lithium doping of a pentacene molecule semiconductor. *Appl. Phys. Lett.*, 86(26):261909–3, 2005.

[72] B. Fang, H. Zhou, and I. Honma. Electrochemical hydrogen storage in Li-doped pentacene. *J. Chem. Phys.*, 124(20):204718–4, 2006.

[73] M. Ahles, R. Schmechel, and H. von Seggern. n-type organic field-effect transistor based on interface-doped pentacene. *Appl. Phys. Lett.*, 85(19):4499–4501, 2004.

[74] S. Lee, B. Koo, J. Shin, E. Lee, H. Park, and H. Kim. Effects of hydroxyl groups in polymeric dielectrics on organic transistor performance. *Appl. Phys. Lett.*, 88(16):162109–3, 2006.

[75] M.-Y. Kuo, H.-Y. Chen, and I. Chao. Cyanation: Providing a three-in-one advantage for the design of n-type organic field-effect transistors. *Chem. - A Euro. J.*, 13(17):4750–4758, 2007.

[76] N. Koch, A. Vollmer, S. Duhm, Y. Sakamoto, and T. Suzuki. The effect of fluorination on pentacene/gold interface energetics and charge reorganization energy. *Adv. Mat.*, 19(1):112–116, 2007.

[77] A. Hepp, H. Heil, R. Schmechel, and H. von Seggern. Electrochemical interface doping in organic light emitting field effect transistors. *Adv. Eng. Mat.*, 7(10): 957–960, 2005.

[78] J.B. Koo, S.J. Yun, J.W. Lim, S.H. Kim, C.H. Ku, S.C. Lim, J.H. Lee, and T. Zyung. Low-voltage and high-gain pentacene inverters with plasma-enhanced atomic-layer-deposited gate dielectrics. *Appl. Phys. Lett.*, 89(3): 033511–3, 2006.

[79] M.-m. Ling, Z. Bao, P. Erk, M. Koenemann, and M. Gomez. Complementary inverter using high mobility air-stable perylene di-imide derivatives. *Appl. Phys. Lett.*, 90(9):093508–3, 2007.

[80] S. Horiuchi, T. Hasegawa, and Y. Tokura. Neutral-ionic transition, ferroelectricity, and field-effect transistors based on molecular donor-acceptor compounds. *Mol. Crys. and Liqu. Crys.*, 455(1):295–304, 2006.

[81] T.-F. Guo, Z.-J. Tsai, S.-Y. Chen, T.-C. Wen, and C.-T. Chung. Influence of polymer gate dielectrics on n-channel conduction of pentacene-based organic field-effect transistors. *J. Appl. Phys.*, 101(12):124505–4, 2007.

[82] Y. Takahashi, T. Hasegawa, Y. Abe, Y. Tokura, and G. Saito. Organic metal electrodes for controlled p- and n-type carrier injections in organic field-effect transistors. *Appl. Phys. Lett.*, 88(7):073504–3, 2006.

[83] H. Nakanotani, M. Yahiro, C. Adachi, and K. Yano. Ambipolar field-effect transistor based on organic-inorganic hybrid structure. *Appl. Phys. Lett.*, 90 (26):262104–3, 2007.

[84] R. Schmechel, M. Ahles, and H. von Seggern. A pentacene ambipolar transistor: Experiment and theory. *J. Appl. Phys.*, 98(8):084511–6, 2005.

[85] S. Sanvito and A.R. Rocha. Molecular-spintronics: The art of driving spin through molecules. *J. Comp. and Theo. Nanoscience*, 2:624–642, 2006.

[86] W.J.M. Naber, S. Faez, and W.G. van der Wiel. Organic spintronics. *J. Phys. D: App. Phys.*, 40(12):R205–R228, 2007.

[87] J. Stöhr and H.C. Siegmann. *Magnetism - From Fundamentals to Nanoscale Dynamics*. Springer-Verlag Berlin Heidelberg, 2006.

[88] I. Appelbaum, B. Huang, and D.J. Monsma. Electronic measurement and control of spin transport in silicon. *Nature*, 447(7142):295–298, 2007.

[89] A. Fert and H. Jaffrès. Conditions for efficient spin injection from a ferromagnetic metal into a semiconductor. *Phys. Rev. B*, 64(18):184420–9, 2001.

[90] A. Fert, J.-M. George, H. Jaffrès, and R. Mattana. Semiconductors between spin-polarized source and drain. *preprint*, arXiv.org:cond-mat/0612495v1:1, 2006.

[91] Z.G. Yu, M.A. Berding, and S. Krishnamurthy. Spin transport in organics and organic spin devices. *Circ., Dev. and Syst., IEE Proc.*, 152(4):334–339, 2005.

[92] Z. G. Yu, M.A. Berding, and S. Krishnamurthy. Organic magnetic-field-effect transistors and ultrasensitive magnetometers. *J. Appl. Phys.*, 97(2):024510–3, 2005.

[93] D. Kitchen, A. Richardella, J.-M. Tang, M.E. Flatte, and A. Yazdani. Atom-by-atom substitution of Mn in GaAs and visualization of their hole-mediated interactions. *Nature*, 442(7101):436–439, 2006.

[94] C.H. Ahn, A. Bhattacharya, M. Di Ventra, J.N. Eckstein, C.D. Frisbie, M.E. Gershenson, A.M. Goldman, I.H. Inoue, J. Mannhart, A.J. Millis, A.F. Morpurgo, D. Natelson, and J.-M. Triscone. Electrostatic modification of novel materials. *Rev. Mod. Phys.*, 78(4):1185–28, 2006.

[95] J.-E. Rubensson. RIXS dynamics for beginners. *J. Electr. Spec. and Rel. Phenom.*, 110-111:135–151, 2000.

[96] F. de Groot. High-resolution x-ray emission and x-ray absorption spectroscopy. *Chem. Rev.*, 101(6):1779–1808, 2001.

[97] F. Jalilehvand. X-ray absorption spectroscopy, 2007. URL `http://www.chem.ucalgary.ca/research/groups/faridehj/xas.pdf`. Accessed on: Apr. 12, 2008.

[98] A. Nilsson. Spectroscopic techniques, 2007. URL `http://www-ssrl.slac.stanford.edu/nilssongroup/pages/core_spec_xps.html`. Accessed on: Apr. 12, 2008.

[99] D. Nordlund. *Core Level Spectroscopy of Water and Ice*. PhD thesis, Stockholm University, 2004.

[100] S. Leitch. *Spectroscopic Analysis of Selected Silicon Ceramics*. Master's thesis, University of Saskatchewan, 2005.

[101] M.O. Krause and J.H. Oliver. Natural widths of atomic K and L levels, K alpha X-ray lines and several KLL auger lines. *J. Phys. Chem. Ref. Data*, 8 (2):329–338, 1979.

[102] T. Hamilton. *Determining the sp^2/sp^3 Bonding Concentrations of Carbon Films*. Master's thesis, University of Saskatchewan, 2005.

[103] A. Moewes. Soft x-ray fluorescence spectroscopy. Summer School for Synchrotron Radiation, CAMD, LSU, Baton Rouge, USA, 2000.

[104] M. Cavalleri. *Local Structure of Hydrogen-Bonded Liquids*. PhD thesis, Stockholm University, 2004.

[105] D. Attwood. *Soft X-rays and Extreme Ultraviolet Radiation*. Cambridge University Press, 2000.

[106] N. Smith. Science with soft x-rays. *Phys. Today*, 54:29–34, 2001.

[107] Beamline 8.0.1, 2007. URL `http://www.als.lbl.gov/als/techspecs/bl8.0.1.html`. Accessed on: Apr. 12, 2008.

[108] J.J. Jia, T.A. Callcott, J. Yurkas, A.W. Ellis, F.J. Himpsel, M.G. Samant, J. Stöhr, D.L. Ederer, J.A. Carlisle, E.A. Hudson, L.J. Terminello, D.K. Shuh, and R.C.C. Perera. First experimental results from IBM/TENN/TULANE/LLNL/LBL undulator beamline at the advanced light source. *Rev. Sci. Instr.*, 66(2):1394–1397, 1995.

[109] M. Newville. Fundamentals of xafs, 2004. URL `http://xafs.org/Tutorials`. Accessed on: Apr. 12, 2008.

[110] F. Duan and J. Guojun. *Introduction to Condensed Matter Physics: Volume 1*. World Scientific, 2005.

[111] J. Kohanoff. *Electronic Structure Calculations for Solids and Molecules - Theory and Computational Methods*. Cambridge University Press, 2006.

[112] A.P. Sutton. *Electronic Structure of Materials*. Oxford University Press, 1993.

[113] P. Hohenberg and W. Kohn. Inhomogeneous electron gas. *Phys. Rev.*, 136 (3B):B864–B871, 1964.

[114] R.M. Martin. *Electronic Structure - Basic Theory and Practical Methods*. Cambridge University Press, 2004.

[115] P.L. Taylor and O. Heinonen. *A Quantum Approach to Condensed Matter Physics*. Cambridge University Press, 2002.

[116] K. Hermann, L.G.M. Pettersson, M.E. Casida, C. Daul, A. Goursot, A. Koester, E. Proynov, A. St-Amant, and D.R. Salahub. StoBe-deMon version 3.0 (2007).

[117] W. Kutzelnigg, U. Fleischer, and M. Schindler. *NMR-Basic Priniciples and Progress*. Springer-Verlag, Heidelberg, 1990.

[118] S. Huzinaga. Gaussian-type functions for polyatomic systems. I. *J. Chem. Phys.*, 42(4):1293–1302, 1965.

[119] N. Godbout, D.R. Salahub, J. Andzelm, and E. Wimmer. Optimization of Gaussian-type basis sets for local spin density functional calculations. Part I. Boron through neon, optimization technique and validation. *Can. J. Chem.*, 70:560–571, 1992.

[120] R.J. Boyd, J. Wand, and L.A. Eriksson. *Recent Advances in Density Functional Methods - Part I - Chapter 10: The Electron Density as Calculated from Density Functional Theory*. World Scientific, 1995.

[121] L. Triguero, L.G.M. Pettersson, and H. Ågren. Calculations of near-edge x-ray-absorption spectra of gas-phase and chemisorbed molecules by means of density-functional and transition-potential theory. *Phys. Rev. B*, 58(12):8097–8110, 1998.

[122] J.C. Slater and K.H. Johnson. Self-consistent-field Xα cluster method for polyatomic molecules and solids. *Phys. Rev. B*, 5(3):844–853, 1972.

[123] J.C. Slater. *Quantum Theory of Molecules and Solids - Vol. IV*. McGraw-Hill, 1974.

[124] L. Triguero, L.G.M. Pettersson, and H. Ågren. Calculations of x-ray emission spectra of molecules and surface adsorbates by means of density functional theory. *J. Phys. Chem. A*, 102(52):10599–10607, 1998.

[125] L.G.M. Pettersson, U. Wahlgren, and O. Gropen. Effective core potential parameters for first- and second-row atoms. *J. Chem. Phys.*, 86(4):2176–2184, 1987.

[126] A.D. Becke. Density-functional exchange-energy approximation with correct asymptotic behavior. *Phys. Rev. A*, 38(6):3098–3100, 1988.

[127] J.P. Perdew. Density-functional approximation for the correlation energy of the inhomogeneous electron gas. *Phys. Rev. B*, 33(12):8822–8824, 1986.

[128] J.P. Perdew and K. Burke. Comparison shopping for a gradient-corrected density functional. *Int. J. Quant. Chem.*, 57(3):309–319, 1996.

[129] L. Triguero, O. Plashkevych, L.G.M. Pettersson, and H. Ågren. Separate state vs. transition state Kohn-Sham calculations of x-ray photoelectron binding energies and chemical shifts. *J. Electr. Spec. and Rel. Phenom.*, 104(1-3):195–207, 1999.

[130] J.D. Smith, C.D. Cappa, B.M. Messer, W.S. Drisdell, R.C. Cohen, and R.J. Saykally. Probing the local structure of liquid water by x-ray absorption spectroscopy. *J. Phys. Chem. B*, 110(40):20038–20045, 2006.

[131] R.B. Campbell, J.M. Robertson, and J. Trotter. The crystal and molecular structure of pentacene. *Acta Cryst.*, 14(7):705–711, 1961.

[132] D. Holmes, S. Kumaraswamy, A.J. Matzger, and K.P.C. Vollhardt. On the nature of nonplanarity in the [N]phenylenes. *Chem. - A Euro. J.*, 5(11):3399–3412, 1999.

[133] P. Potera, I. Stefaniuk, and M. Kuźma. Symmetry of the pentacene molecule and classification of electron states studied in the frame of group action on a set. *Centr. Euro. J. Phys.*, 5(2):165–176, 2007.

[134] R.G. Endres, C.Y. Fong, L.H. Yang, G. Witte, and Ch. Woll. Structural and electronic properties of pentacene molecule and molecular pentacene solid. *Comp. Mat. Sci.*, 29(3):362–370, 2004.

[135] K. Lee and J. Yu. Ab initio study of pentacene on Au(001) surface. *Surf. Sci.*, 589(1-3):8–18, 2005.

[136] L. Versluis and T. Ziegler. The determination of molecular structures by density functional theory. The evaluation of analytical energy gradients by numerical integration. *J. Chem. Phys.*, 88(1):322–328, 1988.

[137] Molekel 5.2. Swiss National Supercomputing Centre, 2007. URL `http://www.cscs.ch`. Accessed on: Apr. 12, 2008.

[138] N. Sato, H. Inokuchi, and E.A. Silinsh. Reevaluation of electronic polarization energies in organic molecular crystals. *Chem. Phys.*, 115(2):269–277, 1987.

[139] N.E. Gruhn, D.A. da Silva Filho, T.G. Bill, M. Malagoli, V. Coropceanu, A. Kahn, and J.-L. Brédas. The vibrational reorganization energy in pentacene: Molecular influences on charge transport. *JACS*, 124(27):7918–7919, 2002.

[140] R.W. Godby, M. Schlüter, and L.J. Sham. Accurate exchange-correlation potential for silicon and its discontinuity on addition of an electron. *Phys. Rev. Lett.*, 56(22):2415–2418, 1986.

[141] Y.-H. Kim and A. Gorling. Exact kohn-sham exchange kernel for insulators and its long-wavelength behavior. *Phys. Rev. B*, 66(3):035114–6, 2002.

[142] K. Hummer and C. Ambrosch-Draxl. Electronic properties of oligoacenes from first principles. *Phys. Rev. B*, 72(20):205205–10, 2005.

[143] P. Parisse, L. Ottaviano, B. Delley, and S. Picozzi. First-principles approach to the electronic structure in the pentacene thin film polymorph. *J. Phys: Cond. Mat.*, 19(10):106209–10, 2007.

[144] S.P. Park, S.S. Kim, J.H. Kim, C.N. Whang, and S. Im. Optical and luminescence characteristics of thermally evaporated pentacene films on Si. *Appl. Phys. Lett.*, 80(16):2872–2874, 2002.

[145] S.H. Lim, R. Li, W. Ji, and J. Lin. Effects of nitrogenation on single-walled carbon nanotubes within density functional theory. *Phys. Rev. B*, 76(19): 195406, 2007.

[146] A. Nilsson and L.G.M. Pettersson. Chemical bonding on surfaces probed by x-ray emission spectroscopy and density functional theory. *Surf. Sci. Rep.*, 55 (2-5):49–167, 2004.

[147] M. Alagia, C. Baldacchini, M.G. Betti, F. Bussolotti, V. Carravetta, U. Ekstrom, C. Mariani, and S. Stranges. Core-shell photoabsorption and photoelectron spectra of gas-phase pentacene: Experiment and theory. *J. Chem. Phys.*, 122(12):124305–6, 2005.

[148] H. Ding and Y. Gao. Alkali metal doping and energy level shift in organic semiconductors. *Appl. Surf. Sci.*, 252(11):3943–3947, 2006.

[149] S. Kera, M.B. Casu, A. Scholl, T. Schmidt, D. Batchelor, E. Ruhl, and E. Umbach. High-resolution inner-shell excitation spectroscopy of H_2-phthalocyanine. *J. Chem. Phys.*, 125(1):014705, 2006.

[150] P. Blaha, K. Schwarz, G.K.H. Madsen, D. Kvasnicka, and J. Luitz. WIEN2k. Vienna University of Technology, 2001.

[151] G. Kresse and J. Furthmüller. Efficient iterative schemes for ab initio total-energy calculations using a plane-wave basis set. *Phys. Rev. B*, 54(16):11169–11186, 1996.

[152] K. Hummer and C. Ambrosch-Draxl. Oligoacene exciton binding energies: Their dependence on molecular size. *Phys. Rev. B*, 71(8):081202–4, 2005.

[153] C.C. Mattheus, G.A. de Wijs, R.A. de Groot, and T.T.M. Palstra. Modeling the polymorphism of pentacene. *JACS*, 125(20):6323–6330, 2003.

[154] J. Repp, G. Meyer, S. Paavilainen, F.E. Olsson, and M. Persson. Imaging bond formation between a gold atom and pentacene on an insulating surface. *Science*, 312(5777):1196–1199, 2006.

[155] J. Huang and M. Kertesz. Validation of intermolecular transfer integral and bandwidth calculations for organic molecular materials. *J. Chem. Phys.*, 122 (23):234707–9, 2005.

[156] G.A. de Wijs, C.C. Mattheus, R.A. de Groot, and T.T.M. Palstra. Anisotropy of the mobility of pentacene from frustration. *Synth. Met.*, 139(1):109–114, 2003.

[157] K. Hannewald, V.M. Stojanovic, J.M.T. Schellekens, P.A. Bobbert, G. Kresse, and J. Hafner. Theory of polaron bandwidth narrowing in organic molecular crystals. *Phys. Rev. B*, 69(7):075211–7, 2004.

[158] L. Tsetseris and S. T. Pantelides. Intercalation of oxygen and water molecules in pentacene crystals: First-principles calculations. *Phys. Rev. B*, 75(15): 153202–4, 2007.

Appendix A

Atomic Structures

All of the atomic coordinates for the molecules used in the StoBe calculations are given in the tables below. The values are in units of angstrom (Å), and are taken after the geometry optimization run was performed.

Table A.1: xyz coordinates for pentacene

Element	x-coordinate (Å)	y-coordinate (Å)	z-coordinate (Å)
C1	1.634	5.653	0.000
C2	2.312	6.851	-0.001
C3	3.733	4.396	0.002
C4	3.756	6.893	0.000
C5	2.355	4.407	0.001
C6	4.491	5.623	0.002
C7	4.472	8.097	-0.001
C8	5.896	8.128	0.001
C9	6.624	9.339	0.000
C10	6.632	6.857	0.004
C11	5.892	5.641	0.004
C12	8.038	9.364	0.002
C13	8.773	8.092	0.007
C14	8.045	6.882	0.007
C15	10.197	8.123	0.011
C16	10.913	9.327	0.010
C17	12.357	9.368	0.014
C18	10.179	10.596	0.004
C19	10.938	11.824	0.003
C20	8.778	10.580	0.001
C21	13.036	10.566	0.013
C22	12.315	11.812	0.007
H1	1.764	7.798	-0.001
H2	0.540	5.638	-0.001
H3	1.796	3.467	0.000
H4	4.280	3.448	0.003
H5	6.440	4.692	0.006
H6	3.925	9.045	-0.002
H7	6.077	10.287	-0.003
H8	8.230	11.528	-0.003
H9	10.391	12.772	-0.001
H10	12.875	12.751	0.006
H11	14.130	10.580	0.016
H12	12.905	8.421	0.018
H13	10.743	7.174	0.015
H14	8.592	5.933	0.011

Table A.2: xyz coordinates for Mn-doped pentacene

Element	x-coordinate (Å)	y-coordinate (Å)	z-coordinate (Å)
Mn	2.978	5.565	1.377
C1	1.467	5.582	-0.057
C2	2.191	6.821	-0.094
C3	3.613	4.331	-0.183
C4	3.634	6.841	-0.209
C5	2.181	4.334	-0.110
C6	4.364	5.569	-0.247
C7	4.387	8.055	-0.106
C8	5.795	8.077	-0.100
C9	6.534	9.276	-0.042
C10	6.526	6.800	-0.138
C11	5.794	5.600	-0.183
C12	7.957	9.304	-0.029
C13	8.682	8.035	-0.064
C14	7.936	6.828	-0.113
C15	10.086	8.055	-0.041
C16	10.826	9.264	0.016
C17	12.250	9.287	0.045
C18	10.108	10.520	0.049
C19	10.856	11.728	0.107
C20	8.688	10.499	0.024
C21	12.947	10.485	0.105
C22	12.244	11.714	0.135
H1	1.652	7.766	0.000
H2	0.382	5.588	0.052
H3	1.637	3.390	-0.034
H4	4.155	3.382	-0.158
H5	6.336	4.648	-0.183
H6	3.840	9.003	-0.047
H7	5.992	10.228	-0.009
H8	8.147	11.453	0.048
H9	10.315	12.681	0.131
H10	12.799	12.656	0.181
H11	14.041	10.483	0.128
H12	12.791	8.335	0.021
H13	10.631	7.104	-0.067
H14	8.482	5.877	-0.134

Appendix B

STOBE Input Files

Given below is an example input file used for StoBe. It gives a list of the xyz-coordinates used for all the atoms and a breakdown of the basis sets used. The auxiliary basis sets are listed first, followed by the orbital basis sets. For XAS calculations the pseudopotentials are then listed, and finally the augmented basis set for the excited state is given. This example shows the input file for an XAS calculation where the alpha orbital (orbital #6) for the first carbon atom (C1) is being excited.

```
#!/bin/csh -f
ln -s ../../../Basis/baslib.new7 fort.3
ln -s ../../../Basis/symbasis.new fort.4
cat >help.inp <<.
TITLE
Mn doped Pentacene C XAS: atom C1 alpha - excited orbital: 6
NOSY
CARTESIAN angstrom
## Element   x-Coord.       y-Coord.       z-Coord.     At.# ##
C1          1.46720403     5.58192079    -0.05679830     6.0
C2          2.19062983     6.82090705    -0.09424891     4.0
C3          3.61336144     4.33114582    -0.18317411     4.0
C4          3.63404126     6.84127495    -0.20918599     4.0
C5          2.18081722     4.33361709    -0.10979751     4.0
C6          4.36355665     5.56914896    -0.24729356     4.0
C7          4.38681544     8.05509299    -0.10603308     4.0
C8          5.79492310     8.07705816    -0.09955240     4.0
C9          6.53417495     9.27564648    -0.04171578     4.0
C10         6.52556989     6.80049744    -0.13815350     4.0
C11         5.79441451     5.60017396    -0.18318107     4.0
C12         7.95660336     9.30427630    -0.02881917     4.0
C13         8.68224940     8.03541218    -0.06410795     4.0
C14         7.93607579     6.82794482    -0.11272253     4.0
C15        10.08561521     8.05516365    -0.04148785     4.0
C16        10.82634003     9.26354589     0.01587426     4.0
C17        12.24964783     9.28732700     0.04450062     4.0
C18        10.10819679    10.51996030     0.04870974     4.0
C19        10.85585807    11.72803045     0.10715064     4.0
C20         8.68797467    10.49932404     0.02422800     4.0
C21        12.94733266    10.48515001     0.10454006     4.0
C22        12.24392099    11.71433147     0.13537732     4.0
```

```
Mn          2.97795300     5.56520860     1.37724088    25.0
H1          1.65158103     7.76635643    -0.00024757     1.0
H2          0.38157147     5.58814824     0.05177295     1.0
H3          1.63746228     3.39045426    -0.03417220     1.0
H4          4.15485569     3.38243529    -0.15816116     1.0
H5          6.33583614     4.64762591    -0.18264257     1.0
H6          3.83988781     9.00256028    -0.04701978     1.0
H7          5.99241234    10.22816386    -0.00929944     1.0
H8          8.14702242    11.45282672     0.04777457     1.0
H9         10.31504453    12.68060665     0.13089200     1.0
H10        12.79877745    12.65578740     0.18127974     1.0
H11        14.04067846    10.48303874     0.12833551     1.0
H12        12.79062473     8.33530619     0.02058111     1.0
H13        10.63061731     7.10408918    -0.06690215     1.0
H14         8.48185225     5.87744241    -0.13444083     1.0
END
RUNTYPE startup
SCFTYPE direct
POTENTIAL nonlocal be88 pd86
GRID fine
MULTIPLICITY 2
VIRT all
CHARGE 0
MAXCYCLES 2000
ECONVERGENCE 0.000001
DCONVERGENCE 0.000001
DMIXING mdens 0.10
DIIS off
ORBI 5d
FSYM scfocc excited
ALFA 65
BETA 64
SYM 1
ALFA 0 1 6 0.5
BETA 0 0
END
XRAY xas
REMTHRESHOLD  1.D-6
END
DOSOUTPUT mulliken
END
### Auxiliary basis sets  ###
A-CARBON (5,2;5,2)
A-CARBON (5,2;5,2)
A-CARBON (5,2;5,2)
```

```
A-CARBON (5,2;5,2)
A-CARBON (5,2;5,2)
A-CARBON (5,2;5,2)
A-CARBON (5,2;5,2)
A-CARBON (5,2;5,2)
A-CARBON (5,2;5,2)
A-CARBON (5,2;5,2)
A-CARBON (5,2;5,2)
A-CARBON (5,2;5,2)
A-CARBON (5,2;5,2)
A-CARBON (5,2;5,2)
A-CARBON (5,2;5,2)
A-CARBON (5,2;5,2)
A-CARBON (5,2;5,2)
A-CARBON (5,2;5,2)
A-CARBON (5,2;5,2)
A-CARBON (5,2;5,2)
A-CARBON (5,2;5,2)
A-CARBON (5,2;5,2)
A-MANGANESE (5,5;5,5)
A-HYDROGEN (3,1;3,1)
A-HYDROGEN (3,1;3,1)
A-HYDROGEN (3,1;3,1)
A-HYDROGEN (3,1;3,1)
A-HYDROGEN (3,1;3,1)
A-HYDROGEN (3,1;3,1)
A-HYDROGEN (3,1;3,1)
A-HYDROGEN (3,1;3,1)
A-HYDROGEN (3,1;3,1)
A-HYDROGEN (3,1;3,1)
A-HYDROGEN (3,1;3,1)
A-HYDROGEN (3,1;3,1)
A-HYDROGEN (3,1;3,1)
A-HYDROGEN (3,1;3,1)
A-HYDROGEN (3,1;3,1)
### Orbital basis sets  ###
O-CARBON iii_iglo
O-CARBON(+4) (311/211/1)
O-CARBON(+4) (311/211/1)
O-CARBON(+4) (311/211/1)
O-CARBON(+4) (311/211/1)
O-CARBON(+4) (311/211/1)
O-CARBON(+4) (311/211/1)
O-CARBON(+4) (311/211/1)
O-CARBON(+4) (311/211/1)
O-CARBON(+4) (311/211/1)
```

```
O-CARBON(+4) (311/211/1)
O-CARBON(+4) (311/211/1)
O-CARBON(+4) (311/211/1)
O-CARBON(+4) (311/211/1)
O-CARBON(+4) (311/211/1)
O-CARBON(+4) (311/211/1)
O-CARBON(+4) (311/211/1)
O-CARBON(+4) (311/211/1)
O-CARBON(+4) (311/211/1)
O-CARBON(+4) (311/211/1)
O-CARBON(+4) (311/211/1)
O-CARBON(+4) (311/211/1)
O-CARBON(+4) (311/211/1)
O-MANGANESE (63321/531/311)
O-HYDROGEN (311/1)
O-HYDROGEN (311/1)
O-HYDROGEN (311/1)
O-HYDROGEN (311/1)
O-HYDROGEN (311/1)
O-HYDROGEN (311/1)
O-HYDROGEN (311/1)
O-HYDROGEN (311/1)
O-HYDROGEN (311/1)
O-HYDROGEN (311/1)
O-HYDROGEN (311/1)
O-HYDROGEN (311/1)
O-HYDROGEN (311/1)
O-HYDROGEN (311/1)
### Augmented basis sets  ###
P-CARBON(+4) (3,1:8,0)
P-CARBON(+4) (3,1:8,0)
P-CARBON(+4) (3,1:8,0)
P-CARBON(+4) (3,1:8,0)
P-CARBON(+4) (3,1:8,0)
P-CARBON(+4) (3,1:8,0)
P-CARBON(+4) (3,1:8,0)
P-CARBON(+4) (3,1:8,0)
P-CARBON(+4) (3,1:8,0)
P-CARBON(+4) (3,1:8,0)
P-CARBON(+4) (3,1:8,0)
P-CARBON(+4) (3,1:8,0)
P-CARBON(+4) (3,1:8,0)
P-CARBON(+4) (3,1:8,0)
P-CARBON(+4) (3,1:8,0)
P-CARBON(+4) (3,1:8,0)
P-CARBON(+4) (3,1:8,0)
P-CARBON(+4) (3,1:8,0)
```

```
P-CARBON(+4) (3,1:8,0)
P-CARBON(+4) (3,1:8,0)
P-CARBON(+4) (3,1:8,0)
P-CARBON(+4) (3,1:8,0)
X-FIRST
END
/.
../../../Source/StoBe.x <help.inp >& XAS_C01a.out
mv fort.2 XAS_C01a.res
mv fort.11 XAS_C01a.xas
mv fort.96 XAS_C01a.mtx
mv XAS_C01a.* strucfin.pdb ../XAS_alpha/XAS_C01/
rm help.inp nohup.out strucfin.plt
```